

# Crustal structure beneath the Strait of Juan de Fuca and southern Vancouver Island from seismic and gravity analyses

D. Graindorge,<sup>1</sup> G. Spence,<sup>2</sup> P. Charvis,<sup>1</sup> J. Y. Collot,<sup>1</sup> R. Hyndman,<sup>3</sup> and A. M. Tréhu<sup>4</sup>

Received 8 February 2002; revised 18 April 2003; accepted 16 June 2003; published XX Month 2003.

[1] Wide-angle and vertical incidence seismic data from Seismic Hazards Investigations in Puget Sound (SHIPS), gravity modeling, and seismicity are used to derive two-dimensional crustal models beneath the Strait of Juan de Fuca. The Eocene volcanic Crescent-Siletz terrane is significantly thicker than previously recognized and extends from near the surface to depths of 22 km or greater. For the northern strait, a weak midcrustal reflector, dipping east from 12- to 22-km depth, is inferred from wide-angle reflections. A stronger deeper reflector, dipping eastward from 23- to 36-km depth, is associated with the top of “reflector band E,” a zone of high reflectivity on coincident Multichannel Seismic (MCS) data, interpreted as a shear zone. A high-velocity zone ( $7.60 \pm 0.2 \text{ km s}^{-1}$ ) between these reflectors is interpreted as a localized slice of mantle accreted with the overlying Crescent-Siletz terrane. For the southern strait, no deep high-velocity layer is observed and the E-band reflectivity is weaker than to the north. A strong deep reflector, interpreted as the oceanic Moho dips eastward from 35 to 42 km. Seismicity within the subducting slab occurs mainly above the inferred oceanic Moho. Gravity modeling, constrained by the wide-angle seismic models and seismicity, is consistent with the inferred large thickness of Crescent-Siletz and high-density rocks ( $3030 \text{ kg m}^{-3}$ ) in the lower crust. **INDEX TERMS:** 1219 Geodesy and Gravity: Local gravity anomalies and crustal structure; 3025 Marine Geology and Geophysics: Marine seismics (0935); 8105 Tectonophysics: Continental margins and sedimentary basins (1212); 9350 Information Related to Geographic Region: North America; 8015 Structural Geology: Local crustal structure; **KEYWORDS:** crustal structure, Juan de Fuca Strait and Vancouver Island, wide-angle seismic, Cascadia subduction zone, Crescent-Siletz terrane, deep crustal reflectivity

**Citation:** Graindorge, D., G. Spence, P. Charvis, J. Y. Collot, R. Hyndman, and A. M. Tréhu, Crustal structure beneath the Strait of Juan de Fuca and southern Vancouver Island from seismic and gravity analyses, *J. Geophys. Res.*, 108(0), XXXX, doi:10.1029/2002JB001823, 2003.

## 1. Introduction

[2] Since 1980, numerous seismic reflection-refraction experiments have been conducted across the margin of Oregon, Washington, and British Columbia to explore the complex velocity and tectonic structure of the Cascadia convergent margin [Spence *et al.*, 1985; Green *et al.*, 1986; Taber and Lewis, 1986; Clowes *et al.*, 1987; Calvert and Clowes, 1990, 1991; Hyndman *et al.*, 1990; Tréhu *et al.*, 1994; Calvert, 1996; Miller *et al.*, 1997; Flueh *et al.*, 1998; Parsons *et al.*, 1998, 1999; Gerdomb *et al.*, 2001]. During the Seismic Hazards Investigations in Puget Sound (SHIPS) experiment, conducted in March 1998, onshore-offshore wide-angle data and multichannel reflection data were

collected in northwestern Washington State and southwestern British Columbia [Brocher *et al.*, 1999; Fisher *et al.*, 1999]. The objectives were (1) to define the geometry of deep structures that control earthquake occurrence, including the megathrust fault that produces great earthquakes, (2) to provide detailed controls on seismic velocity crustal structure and on crustal faults, and (3) to define sedimentary basins that may affect strong motions during earthquakes.

[3] In this paper we present combined seismic and gravity analyses around the Strait of Juan de Fuca, a 100-km long and 20–25 km wide west-northwest oriented topographic depression, which separates Vancouver Island from the Olympic Peninsula. The analyses are aimed at (1) resolving the velocity structure and thickness of sedimentary basins [Fisher *et al.*, 1999] and the Eocene oceanic Crescent-Siletz terrane, which may be thicker than previously recognized and is thought to be composed of strong crustal blocks of oceanic origin that play an important role in crustal deformation [Tréhu *et al.*, 1994; Stanley and Villaseñor, 2000; Ramachandran, 2001]; (2) constraining the nature of lower crust high-velocity zones [Spence *et al.*, 1985; Drew and Clowes, 1990] and a large reflector band called E that has been interpreted to be a present or former decollement [Yorath *et al.*, 1985; Calvert, 1996; Green *et al.*, 1986; 67

<sup>1</sup>UMR Géosciences Azur, Observatoire Océanologique de Villefranche sur Mer, Quai de la Darse, Villefranche sur Mer, France.

<sup>2</sup>School of Earth and Ocean Sciences, University of Victoria, Victoria, British Columbia, Canada.

<sup>3</sup>Pacific Geoscience Center, Geological Survey of Canada, Sidney, British Columbia, Canada.

<sup>4</sup>College of Oceanic and Atmospheric Sciences, Oregon State University, Corvallis, Oregon, USA.

68 *Clowes et al.*, 1987; *Hyndman*, 1988; *Calvert and Clowes*,  
69 1990; *Hyndman et al.*, 1990]; and (3) determining the  
70 geometry of the downgoing oceanic crust and mantle  
71 [*Calvert*, 1996] by comparing our results with local micro-  
72 earthquakes. This study using wide-angle data will then test  
73 previous interpretations of Crescent-Siletz terrane thickness,  
74 of the E reflection and of the geometry of the Moho  
75 reflections on the Multichannel Seismic (MCS) data.

76 [4] This paper complements a regional seismic tomogra-  
77 phy study [*Ramachandran*, 2001] and MCS data recorded  
78 along coincident lines [*Tréhu et al.*, 2002]. Two-dimensional  
79 velocity models along the Strait of Juan de Fuca were  
80 obtained using simultaneous inversion of travel times from  
81 marine air gun shots recorded on land stations. The velocity  
82 models are used as constraints to interpret coincident MCS  
83 sections, to carry out gravity analyses, and to analyze the  
84 relation of the structure to the seismicity distribution in three  
85 dimensions.

## 86 2. Geological and Tectonic Setting

### 87 2.1. Plate Tectonic Setting

88 [5] The Cascadia continental margin extends from north-  
89 ern California to southern British Columbia (Figure 1). It is  
90 associated with the Cascadia magmatic arc onshore and the  
91 subducting Juan de Fuca and Gorda plates offshore  
92 (Figure 1). Convergence has been the dominant mode of  
93 plate interaction along western margin of North America for  
94 the past 150 Ma [*Engebretson et al.*, 1992]. Exotic material  
95 has been accreted to the margin and then sheared northward  
96 during successive episodes of northeast directed oblique  
97 convergence and transform motion [e.g., *Riddiough*,  
98 1982]. Two narrow terranes, the Mesozoic mainly sediment-  
99 ary Pacific Rim and the Eocene volcanic Crescent-Siletz  
100 [*Brandon*, 1989], were successively emplaced along the  
101 coast at the time of North Pacific plate reorganization  
102 at 43 Ma (Figure 2). Currently, the northern Juan de Fuca  
103 plate subducts beneath North America at a relative rate of  
104 40–47 mm a<sup>-1</sup> directed N56°–68°E [*DeMets et al.*, 1990;  
105 *Riddiough and Hyndman*, 1991] (Figure 1).

### 106 2.2. Regional Geological and Geophysical Setting

107 [6] The basic crustal structure in the Vancouver Island  
108 region has been investigated in a variety of geological and  
109 geophysical studies. Vancouver Island is underlain mainly  
110 by rocks of the Wrangellia terrane (part of the Insular  
111 superterrane), an accreted package of Devonian through  
112 Lower Jurassic igneous sequences, and sedimentary succes-  
113 sions [*Wheeler et al.*, 1989; *Journey and Friedman*, 1993].  
114 On southern Vancouver Island, the Pacific Rim terrane is a  
115 metamorphic sediment-rich mélange unit in contact with  
116 Wrangellia rocks along the San Juan-Survey fault system  
117 (Figure 2).

118 [7] Crescent formation (also known as Siletz River Vol-  
119 canics in Oregon and as Metchosin formation on southern  
120 Vancouver Island [*Snively et al.*, 1968; *Massey*, 1986;  
121 *Tréhu et al.*, 1994]), which comprises voluminous subma-  
122 rine and subaerial basalts of tholeiitic composition with  
123 minor amounts of alkali basalt [*Glasse*, 1974; *Babcock et*  
124 *al.*, 1992], is found at the southern tip of Vancouver Island  
125 and the northern Olympic Peninsula (Figure 2). This terrane  
126 is thought to have formed as either an accreted oceanic

127 island or a seamount chain [*Duncan*, 1982] or as an accreted  
128 oceanic plateau or to have formed in place as the product of  
129 a hot spot generated during a continental margin-rifting  
130 event [*Babcock et al.*, 1992]. The Pacific Rim and Crescent  
131 terranes are separated by the Leech River Fault (Figure 2).  
132 In central Oregon, Crescent-Siletz volcanics are 25–35 km  
133 thick [*Tréhu et al.*, 1994]. This terrane is thought to thin  
134 progressively northward into Washington, where its mapped  
135 thickness is more than 16 km [*Babcock et al.*, 1992]. The  
136 Crescent-Siletz terrane extends to depths as great as 25 km  
137 based on tomographic results [*Symons and Crosson*, 1997;  
138 *Van Wagoner et al.*, 2002]. It has previously been inter-  
139 preted as only 6 km thick offshore Vancouver Island  
140 [*Hyndman et al.*, 1990]. Crescent-Siletz terrane provides  
141 the backstop to a large accretionary sedimentary prism  
142 formed from the sediments scraped off the incoming oceanic  
143 plate [*Brandon and Calderwood*, 1990; *Hyndman*,  
144 1995b; *Parsons et al.*, 1999; *Stanley et al.*, 1999] (Figure 2).

145 [8] An important feature of the lower crust beneath  
146 Vancouver Island, first detected on Lithoprobe Vibroseis  
147 seismic reflection lines across Vancouver Island, is a 5–8 km  
148 thick band of high reflectivity which dips eastward from  
149 around 20 to 33 km depth [*Yorath et al.*, 1985] (Figure 2).  
150 There have been a variety of subduction-related interpreta-  
151 tions for the origin of this reflective layer, generally referred  
152 to as the “E” reflectivity band. *Calvert and Clowes* [1990]  
153 and *Calvert* [1996] argue that it is a structural feature  
154 associated with a lower crustal shear zone, while *Hyndman*  
155 [1988] and *Kurtz et al.* [1990] suggest that the reflectivity  
156 is produced by fluid-filled porosity within sediment or  
157 mafic materials that have been deeply subducted.

158 [9] Velocities >7.0 km s<sup>-1</sup> have been interpreted by  
159 *Spence et al.* [1985] to overlie the lower crustal reflective  
160 band. Beneath Vancouver Island several interpretations for  
161 the high-velocity zone have been proposed, including (1) a  
162 detached piece of oceanic lithosphere accreted during an  
163 episodic event [*Green et al.*, 1986] and (2) imbricated mafic  
164 rocks derived from the top of the subducting oceanic crust  
165 by continuous accretion [*Clowes et al.*, 1987; *Fuis*, 1998].

### 166 2.3. Seismicity

167 [10] In the past century, few subduction zones have  
168 exhibited such low recurrence rates for large earthquakes  
169 as Cascadia. Prior to the  $M_w$  6.8 Nisqually event in 2001  
170 [*Malone et al.*, 2001], no subduction earthquake of moment  
171 magnitude ( $M_w$ ) larger than 6 has occurred there for the past  
172 70 years [*Kanamori and Heaton*, 1996], and no great  
173 interplate event has occurred within recorded history  
174 [*Rogers*, 1988; *Dewey et al.*, 1989]. However, the Cascadia  
175 subduction zone has many characteristics in common with  
176 those along which large interplate earthquakes occur  
177 [*Heaton and Hartzell*, 1987; *Rogers*, 1988]. Furthermore,  
178 many lines of evidence provide strong support for the  
179 occurrence of great thrust events at an average interval  
180 of 600 years, with the last event occurring in 1700  
181 [*Atwater*, 1987, 1992, *Hyndman*, 1995a; *Satake et al.*,  
182 1996; *Goldfinger et al.*, 1999] (Figure 1). Most current  
183 seismicity in the Cascadia forearc of southern British  
184 Columbia and Washington is concentrated around Puget  
185 Sound and the eastern Strait of Juan de Fuca [*Ludwin et al.*,  
186 1991]. The margin seismicity includes (1) events within the  
187 continental crust occurring in the Puget Sound-Georgia

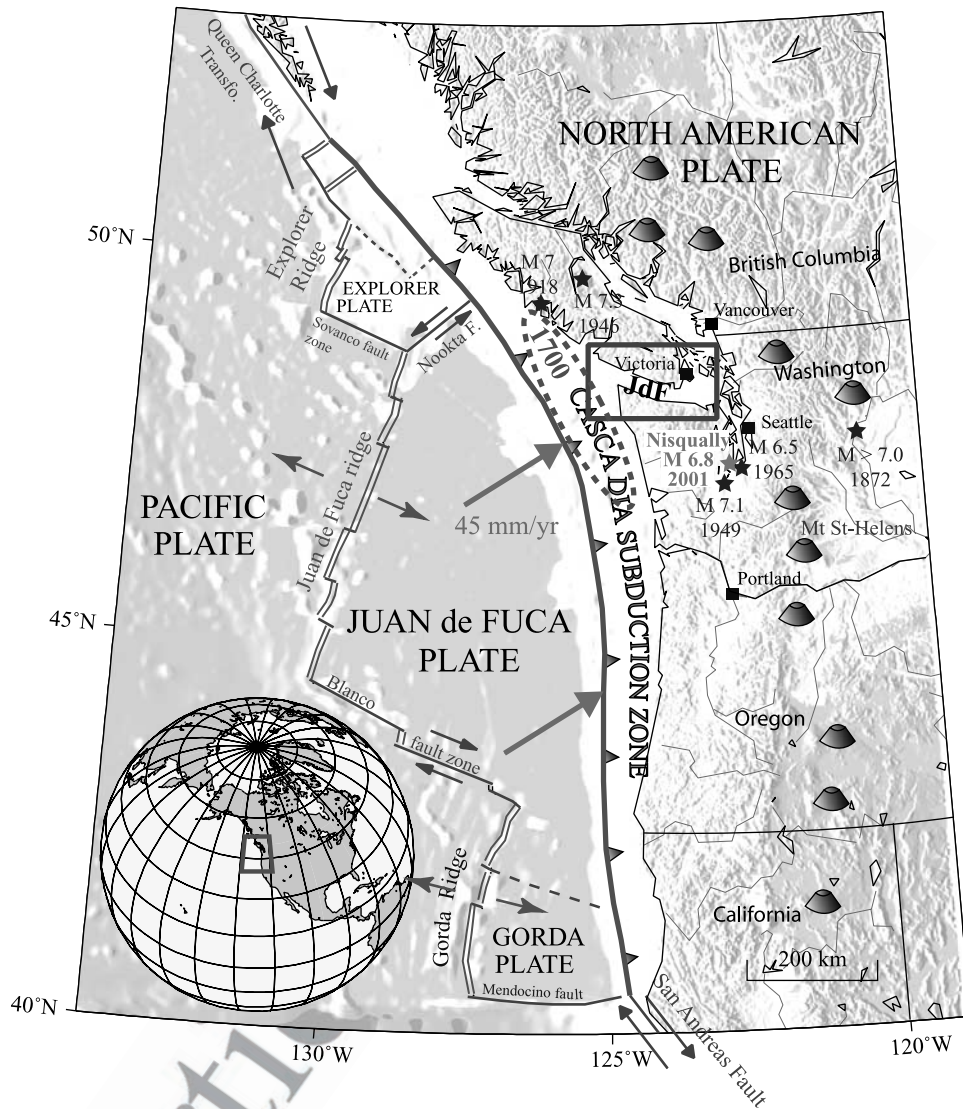


**Figure 1.** Map of the Cascadia Subduction Zone showing the Juan de Fuca plate offshore and the volcanic arc on the North American plate. Stars indicate the largest earthquakes recorded. The ellipse indicates the rupture zone of the inferred 1700 large earthquake. The rectangle delimits the study area around the Strait of Juan de Fuca.

188 Strait area, associated with north-south shortening that  
 189 accommodates arc-parallel migration of an Oregon forearc  
 190 block in response to oblique subduction [Wang, 1996; Wells  
 191 *et al.*, 1998; Khazaradze *et al.*, 1999; Mazzotti *et al.*, 2002]  
 192 and (2) Benioff zone earthquakes.

### 194 3. Data

#### 195 3.1. Seismic Data

##### 196 3.1.1. Wide-Angle Data

197 [11] The wide-angle data presented here were recorded  
 198 during the 1998 SHIPS experiment. SHIPS was conducted  
 199 within and near Puget Sound, the Strait of Juan de Fuca,  
 200 Hood Canal, and Georgia Strait (Figure 1). The R/V  
 201 *Thomas G. Thompson* towed the air gun sources and  
 202 recorded MCS data [Brocher *et al.*, 1999; Fisher *et al.*,  
 203 1999]. In this study, we interpret data mainly from three  
 204 shot profiles (lines 4, 7, and 8) fired along the Strait of

Juan de Fuca (Figure 2). During wide-angle surveying, a  
 205 110 L array was fired approximately every 40 s (line 4),  
 206 while during the MCS survey, an 85 L array was fired  
 207 every 20 s (lines 7 and 8). DFS-V field recording instru-  
 208 ments were used to collect 24-fold, 16 s data from the 96-  
 209 channel, 2500-m streamer [Fisher *et al.*, 1999]. The large  
 210 air gun arrays were recorded by more than 250 onland  
 211 seismographs. Stations were REFTEK recorders contain-  
 212 ing either an oriented three components or a single  
 213 vertical seismometer [Brocher *et al.*, 1999]. Reftek station  
 214 locations and elevations are given by Brocher *et al.*  
 215 [1999]. Table 1 provides a list of station names used in  
 216 this study versus their names in the work by Brocher *et al.*  
 217 [1999].  
 218

[12] We selected recorders located near the ship's tracks  
 219 to provide quasi two-dimensional lines, although the  
 220 curvature of the waterways precluded purely linear profiles  
 221 [Brocher *et al.*, 1999]. For this study, we used five stations  
 222

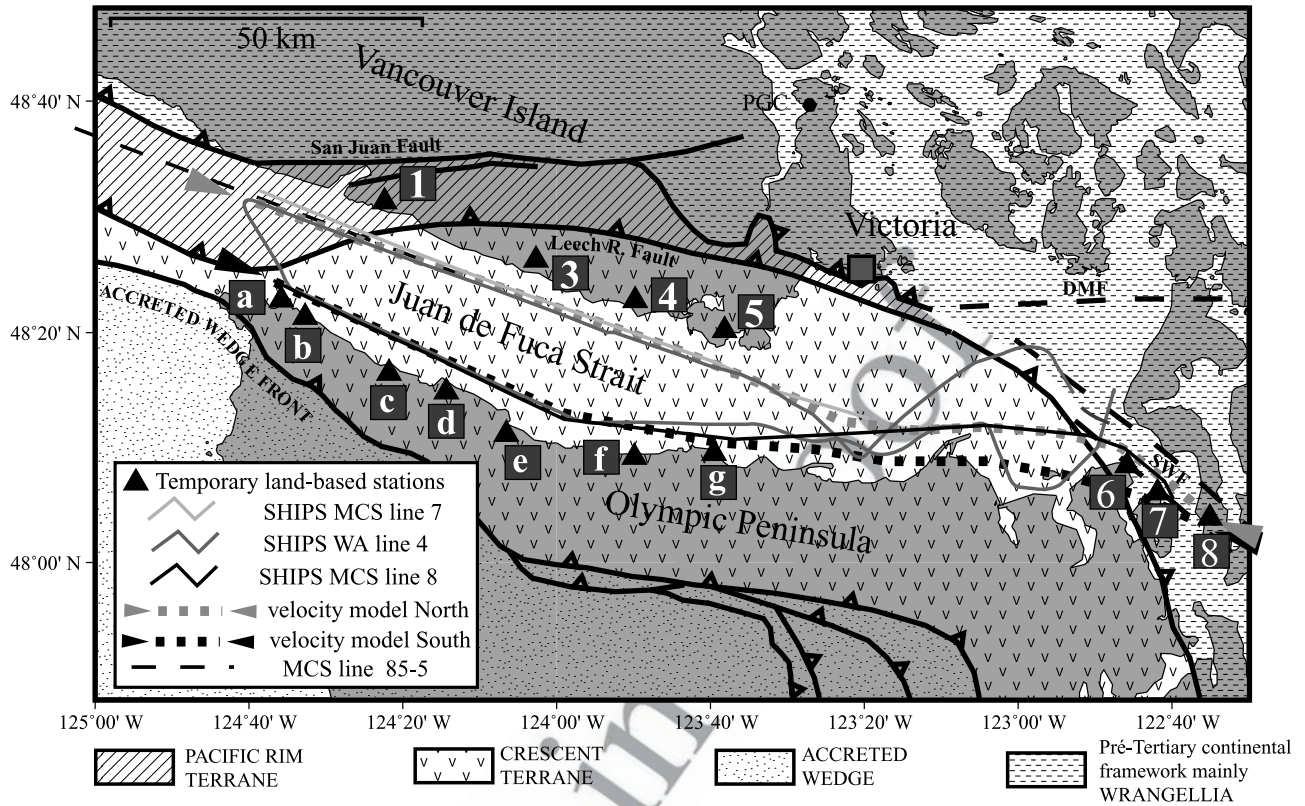


**Figure 2.** Principal geological units in study: accreted wedge, Crescent terrane, Pacific Rim terrane, and pre-Tertiary continental framework. The triangles are locations of land-based stations used in the travel time modeling of wide-angle arrivals. Shaded lines indicate MCS profiles, and ship track lines of the SHIPS indicate seismic reflection survey. DMF, Devils Mountain Fault; SWF, Southern Whidbey Island Fault.

223 from southern Vancouver Island, seven stations from  
 224 northern and northeastern Olympic Peninsula, and three  
 225 stations from northern Puget Sound. To reduce three-  
 226 dimensional effects, we ignored all arrivals with an offset  
 227 less than 7 km. We kept 20 s of the signal of the vertical  
 228 component of data with the time of the first sample  
 229 controlled by offset and a reducing velocity of 8 km s<sup>-1</sup>.  
 230 A Butterworth band-pass filter with limits of 5 and 15 Hz  
 231 was applied. The amplitude of each trace was normalized  
 232 by the square root of offset.

233 [13] We applied a small single static shift to each profile  
 234 to correct for the differing elevations of each receiver  
 235 station. A limitation of the two-dimensional modeling  
 236 approach for this type of onshore-offshore data set is that  
 237 the receiver and the nearest shots are at the same position in  
 238 the model, but the receiver is on land and the shots are in  
 239 water. Thus we applied a correction that substituted a water  
 240 layer (velocity 1.5 km s<sup>-1</sup>) for the equivalent layer of solid  
 241 rock that lay beneath the receiver. All stations were on or  
 242 near bedrock, so we assumed a near-surface rock velocity of  
 243 6 km s<sup>-1</sup>, based on the near-offset apparent velocities on the  
 244 recorded profiles. For the correction, we assumed a phase  
 245 velocity of 6.5 km s<sup>-1</sup>, approximately the mean of the  
 246 observed phase velocities that ranged from 6.0 to 7.2  
 247 km s<sup>-1</sup>. For each station, the static correction simulates a  
 248 model in which the receiver is located in water at sea  
 249 level, with water depth given by the depth at the closest

shot. A typical correction was 120 ms, and so errors in the  
 250 assumptions will result in uncertainties that are much less  
 251 than the smallest picking error of 50 ms.

**3.1.2. Wide-Angle Modeling Procedure**

[14] The velocity models were developed through a  
 254 combination of travel time inversion and amplitude model-  
 255 ing of both wide-angle reflections and refractions. Empirical  
 256 raytrace forward modeling was first applied to get an  
 257

**Table 1.** List of Station Names Used in This Study Versus Their Names as Given by Brocher et al. [1999]

Stations Names Used in This Study	Station Names Given by Brocher et al. [1999]	t1.1	t1.2
1	CA01		t1.3
2	CA02		t1.4
3	CA03		t1.5
4	CA04		t1.6
5	CA05		t1.7
6	OR03		t1.8
7	OR01		t1.9
8	1016		t1.10
A	OR25		t1.11
B	OR24		t1.12
C	OR22		t1.13
D	OR21		t1.14
E	OR19		t1.15
F	OR17		t1.16
G	OR14		t1.17

t2.1 **Table 2.** Observed Phases and Travel Time Fits for Deep-Crustal Northern Model

Layer	Phases	Instruments	Pick Uncertainty, s	Travel Time Fits			
				Number of Travel Times	RMS Misfit, s	Normalized $\chi^2$	
t2.4	3	<i>P1</i>	7, 8	0.050	261	0.084	1.951
t2.5	4	<i>Pg</i>	1, 3, 4, 5, 6, 7, 8	0.070	4698	0.128	3.35
t2.6	4	<i>Pr1</i>	1, 3, 4, 5, 6, 7, 8	0.200	802	0.201	1.012
t2.7	5	<i>Pr2</i>	1, 3, 4, 5, 6, 7, 8	0.150	1591	0.202	1.822

258 acceptable starting model that roughly matches the observed  
 259 and calculated travel times. The travel times were then  
 260 inverted using the raytrace-based inversion scheme of *Zelt*  
 261 *and Smith* [1992]. This inversion is performed in a layer-  
 262 stripping fashion, where the parameters of successively  
 263 deeper layers are determined while the parameters defining  
 264 the shallower layers remain fixed. First, arrival and reflec-  
 265 tion travel times recorded on the land stations were digi-  
 266 tized, and uncertainties which depend on signal-to-noise  
 267 ratios were estimated (Tables 2 and 3).

268 [15] The hybrid procedure used to derive models consisted  
 269 of (1) determination of the water depth and sediment layer  
 270 thicknesses from coincident MCS data (we used a mean  
 271 velocity of  $2.2 \text{ km s}^{-1}$  since the average sediment velocities  
 272 determined from travel times of the near-offset arrivals  
 273 ranged from  $2.0$  to  $3.5 \text{ km s}^{-1}$ ); (2) travel time inversion  
 274 of upper middle crustal turning waves (phase *Pg*); (3) travel  
 275 time inversion of deeper reflected arrivals; and (4) adjustment  
 276 of the velocity contrasts across the midcrust to lower crust  
 277 reflectors via amplitude modeling and subsequent iteration  
 278 through the travel time inversion of steps 2–3.

279 [16] We assessed the quality of the velocity model using  
 280 four measures: the uncertainty of the travel time picks, the  
 281 goodness of fit between predicted and observed travel times,  
 282 the resolution of velocity and interface nodes related to the  
 283 ray coverage (Figures 5 and 10 and Tables 2 and 3), and the  
 284 variability of the model within the model space by com-  
 285 paring Root Mean Squares (RMS) travel time misfits and  $\chi^2$   
 286 values for a suite of velocity models [Holbrook *et al.*, 1994;  
 287 *Zelt*, 1999]. The nodes with a resolution value  $>0.5$  are  
 288 considered to be well resolved [Zelt and Smith, 1992]. To  
 289 evaluate the travel time fits,  $T_{rms}$  is the RMS of the misfit  
 290 between the calculated and observed travel times, and its  
 291 value should be as close as possible to the uncertainty of the  
 292 travel time picks. The  $\chi^2$  is a dimensionless value repre-  
 293 senting the RMS of the misfit normalized by the uncertainty  
 294 of the observed travel times; its value should ideally be  
 295 close to 1. These statistical measures, presented in Tables 2  
 296 and 3, indicate that the formal picking errors may be

297 unrealistically small and that the parameterization may not  
 298 be representative of the small-scale variations near the shots  
 299 and receivers. For amplitude modeling, synthetic seismo-  
 300 grams were calculated using zero-order asymptotic ray  
 301 theory [Cerveny *et al.*, 1977]. Modeling of amplitudes  
 302 aimed to fit the general trends of critical point locations  
 303 for specific phases, while modeling of relative amplitudes  
 304 between phases was only qualitative.

### 3.1.3. MCS Data

306 [17] SHIPS MCS lines 7 and 8 (Figure 11) are coincident  
 307 with northern and southern wide-angle models, respectively.  
 308 Only basic processing including geometrical correction and  
 309 deconvolution, sorting into common depth point reflection  
 310 gathers, velocity analysis, Normal Move Out (NMO)  
 311 correction and stacking, and migration have been applied  
 312 thus far to these two MCS lines [Tréhu *et al.*, 2002].  
 313 Recently, more extensive processing has been carried out,  
 314 and a portion of the newly processed data is presented by  
 315 Nedimovic *et al.* [2003]. The westernmost 40 km of SHIPS  
 316 MCS line 7 is coincident with the eastern portion of  
 317 interpreted Lithoprobe Vibroseis line 85-05 [Clowes *et al.*,  
 318 1987].

### 3.2. Seismicity Data

319 [18] Seismicity levels are highest in the eastern Strait of  
 320 Juan de Fuca and Puget Sound [e.g., Weaver and Baker,  
 321 1988]. Microearthquakes around the Strait of Juan de Fuca  
 322 compiled by Mulder [1995; also personal communication,  
 323 2001] are displayed along three sections perpendicular to  
 324 the strait (Figures 12 and 13). We used all the events from  
 325 this catalog with magnitude greater than 1 recorded between  
 326 the years 1984 and 2000 to have enough events to propose a  
 327 hypothetical interpretation of the top of the downgoing plate  
 328 seismicity. Events from 25 km on either side of each section  
 329 were projected perpendicularly onto the line (Figure 12).  
 330 Hypocenter locations were determined using a laterally  
 331 homogeneous model. When earthquakes are relocated in a  
 332 three-dimensional velocity model derived from SHIPS data,  
 333 hypocenters change by less than 3 km horizontally and  
 334

t3.1 **Table 3.** Observed Phases and Travel Time Fits for Deep-Crustal Southern Model

Layer	Phases	Instruments	Pick Uncertainty, s	Travel Time Fits			
				Number of Travel Times	RMS Misfit, s	Normalized $\chi^2$	
t3.4	2	<i>S</i>	d	0.04	20	0.045	1.33
t3.5	3	<i>P1</i>	a, b, c, d, e, f	0.05	149	0.077	2.01
t3.6	3	<i>2r</i>	a, b, c, d	0.250	68	0.252	1.03
t3.7	4	<i>Pg</i>	a, b, c, d, e, f, g	0.07	852	0.135	3.74
t3.8	5	<i>Pr2</i>	a, b, c, d, e, f, g	0.200	195	0.286	2.06
t3.9	Moho, 1: $6.4 \text{ km s}^{-1}$	<i>PmP</i>	a, b, c, d, e	0.07	55	0.085	1.51
t3.10	Moho, 2: $7.1 \text{ km s}^{-1}$	<i>PmP</i>	a, b, c, d, e	0.07	55	0.092	1.77
t3.11	Moho, 3: $7.6 \text{ km s}^{-1}$	<i>PmP</i>	a, b, c, d, e	0.07	56	0.101	2012

335 vertically [Ramachandran, 2001], and so these values  
 336 represent reasonable estimates of absolute hypocenter  
 337 uncertainty for bigger events. However, events with magni-  
 338 tudes ranging from 1.0 to 2.5 are probably fairly poorly  
 339 located since they are only observed on few stations and  
 340 uncertainty in depth is more likely greater than 5 km.

### 341 3.3. Gravity Data

342 [19] Gravity data in the Strait of Juan de Fuca region from  
 343 both the Geological Survey of Canada (GSC) and the U.S.  
 344 Geological Survey were combined in a consistent manner  
 345 by C. Lowe (personal communication, 2001). The nominal  
 346 data spacing is  $\sim 1$  km. Offshore free air data are accurate  
 347 to  $\pm 2$  mGal, and onshore terrain-corrected Bouguer mea-  
 348 surements are accurate to  $\pm 1$  mGal. We modeled gravity  
 349 data along the same three profiles (A, B, C) across the  
 350 Strait of Juan de Fuca used for projection of seismic  
 351 events (Figure 14). We used the program HYPERMAG,  
 352 an interactive, 2 and  $2^{1/2}$  dimensional forward modeling  
 353 program from the U.S. Geological Survey [Saltus and  
 354 Blakely, 1993]. The two-dimensional calculations are based  
 355 on the Talwani algorithm [Talwani et al., 1959]. Gravity  
 356 curves were determined using a 0.3 by 0.3 min gridding of  
 357 the gravity data.

## 359 4. Northern Model

360 [20] The northern model is based on a 164-km-long  
 361 seismic line in the northern and southeastern Strait of Juan  
 362 de Fuca (Figure 2). To determine our velocity model, we  
 363 selected stations from southern Vancouver Island and north-  
 364 ern Puget Sound: stations 1–8 except 2 which was poor.  
 365 Three stations (3–5) lie directly on Crescent-Siletz Terrane.  
 366 The stations were all located near the northern coast of the  
 367 Strait of Juan de Fuca and were typically less than 5 km  
 368 from the air gun line. SHIPS lines 4 and 7 were used for the  
 369 western and the central part of the model and line 8 for the  
 370 eastern part.

### 371 4.1. Wide-Angle Data

372 [21] In some cases, the data quality provided by the  
 373 smaller air gun array used for MCS recording was better  
 374 than that used for the wide-angle recording, probably  
 375 because the MCS air gun array provided a more impulsive  
 376 waveform. The noise level on most northern stations was  
 377 low. Sample records of stations 4 and 5 are shown on  
 378 Figures 3 and 4.

379 [22] Three principal phases are observed on the wide-  
 380 angle data of the northern line: a refraction or turning ray  
 381 within the upper crust ( $P_g$ ) picked out to offsets of 150 km  
 382 and reflections from two deep boundaries ( $Pr1$  and  $Pr2$ ,  
 383 Figures 3 and 4a) which can be consistently correlated on all  
 384 stations. On stations 4 and 5, the  $P_g$  apparent velocity is  
 385  $6\text{--}6.5$  km  $s^{-1}$  and the intercept time is 0.2 s, which demon-  
 386 strates that sediments within the Strait of Juan de Fuca are  
 387 very thin. The high-amplitude first arrivals, which we can  
 388 clearly follow to distances of more than 80 km, are the  
 389 strongest arrivals on the seismic sections. The weak upper  
 390 reflected wave  $Pr1$  is asymptotic to the  $P_g$  refracted arrival at  
 391 a distance of more than 80 km on stations 4 and 5. This  
 392 reflection is interpreted as an arrival from a weak discontinuity  
 393 at midcrustal depths. In addition, an earlier arrival  $P1$

with an apparent velocity of 5 km  $s^{-1}$  from near-surface and  
 shallow depth sediments is observed on stations at the  
 eastern end of the line (Figure 4b). The deeper reflection  
 $Pr2$  has a larger amplitude corresponding to a stronger  
 velocity discontinuity at greater depth. We also observe the  
 $S$  wave arrival ( $S_g$ ) for the upper crustal layer with an  
 apparent velocity of 3.6 km  $s^{-1}$ .

### 401 4.2. Velocity Model

402 [23] Modeling of wide-angle refracted and reflected travel  
 403 times and amplitudes produced a model of compressional  
 404 wave ( $P$ ) velocity of the crust below the northern Strait of  
 405 Juan de Fuca (Figure 5b). Layer 1 represents the seawater.  
 406 The upper to middle crust (layer 4) consists of a thick, high-  
 407 velocity layer ( $6.1\text{--}6.3$  km  $s^{-1}$  at the top of the layer  
 408 increasing to  $7.3\text{--}7.5$  km  $s^{-1}$  at its base at 20–22 km depth  
 409 with a velocity gradient of  $\sim 0.1\text{--}0.15$  km  $s^{-1}$ ). Over the  
 410 first 90 km of the model, layer 4 is overlain by a thin layer  
 411 of sediments (layer 2) with velocities of about 2–3 km  $s^{-1}$   
 412 and with a thickness of a few hundred meters, thickening to  
 413 the southeast. At the southeast end of the line (model  
 414 distance 125–160 km), velocities of about 3 km  $s^{-1}$  are  
 415 found at 3-km depth, below which we can identify a third  
 416 layer (3) with velocities increasing from 4.2–4.6 to 5.5–6.0  
 417 km  $s^{-1}$  at 6-km depth. Reflector  $Pr1$ , deepening eastward  
 418 from 12 to 22 km, represents an interface across which the  
 419 velocity contrast is very small. Reflector  $Pr2$  dips eastward  
 420 from 23 to 36 km. Inferred layer 5 between  $Pr1$  and  $Pr2$ ,  
 421 8–12 km in thickness, is characterized by very high velocities  
 422 ranging from 7.5 to 7.7 km  $s^{-1}$ . There are no constraints on  
 423 velocity structure beneath the deeper reflector ( $Pr2$ ).

### 424 4.3. Model Uncertainty

425 [24] The agreement between observed and predicted  
 426 travel times is generally satisfactory (Figures 3 and 5).  
 427 Travel time RMS residuals (misfits) for individual phases  
 428 (reflected and refracted) range from 0.084 to 0.202 s,  
 429 comparable to the picking errors that range from 0.050 to  
 430 0.200 s (Table 2) (Figure 5a). Amplitudes from synthetic  
 431 seismograms provide an acceptable fit to the data (Figures 3c  
 432 and 3d). Relative amplitudes of phases  $P_g$ ,  $Pr1$ , and  $Pr2$  are  
 433 matched, and location of critical points also fit reasonably  
 434 well. For the  $P_g$  phase, synthetic amplitudes at far offsets  
 435 are too large compared to the observed data, perhaps  
 436 indicating that the deep velocity gradient is too large;  
 437 however, a smaller gradient would produce a larger-than-  
 438 observed  $Pr1$  amplitude. Resolution values for velocity and  
 439 interface nodes were calculated during the inversion of  
 440 travel times [Zelt and Smith, 1992] (Figures 6a and 6b).  
 441 These values together with the number of ray hits  
 442 (Figure 5c) provide an estimate of ray coverage within the  
 443 model and are highly dependent on the model parameteriza-  
 444 tion. Velocities at the top of the basement layer 4 were  
 445 constrained by both refracted and reflected arrivals and have  
 446 resolution values  $>0.75$ . The weakness of the first reflection  
 447  $Pr1$  implies a small velocity contrast between crustal layers  
 448 4 and 5 ( $<0.3$  km  $s^{-1}$ ) based on amplitude modeling  
 449 (Figure 3). Although resolution values are useful indicators,  
 450 insight into uncertainties in velocity and interface depth is  
 451 best obtained by comparing RMS travel time misfits and  $\chi^2$   
 452 values for a suite of velocity models [Holbrook et al., 1994;  
 453 Zelt, 1999]. This analysis is a way to approach model

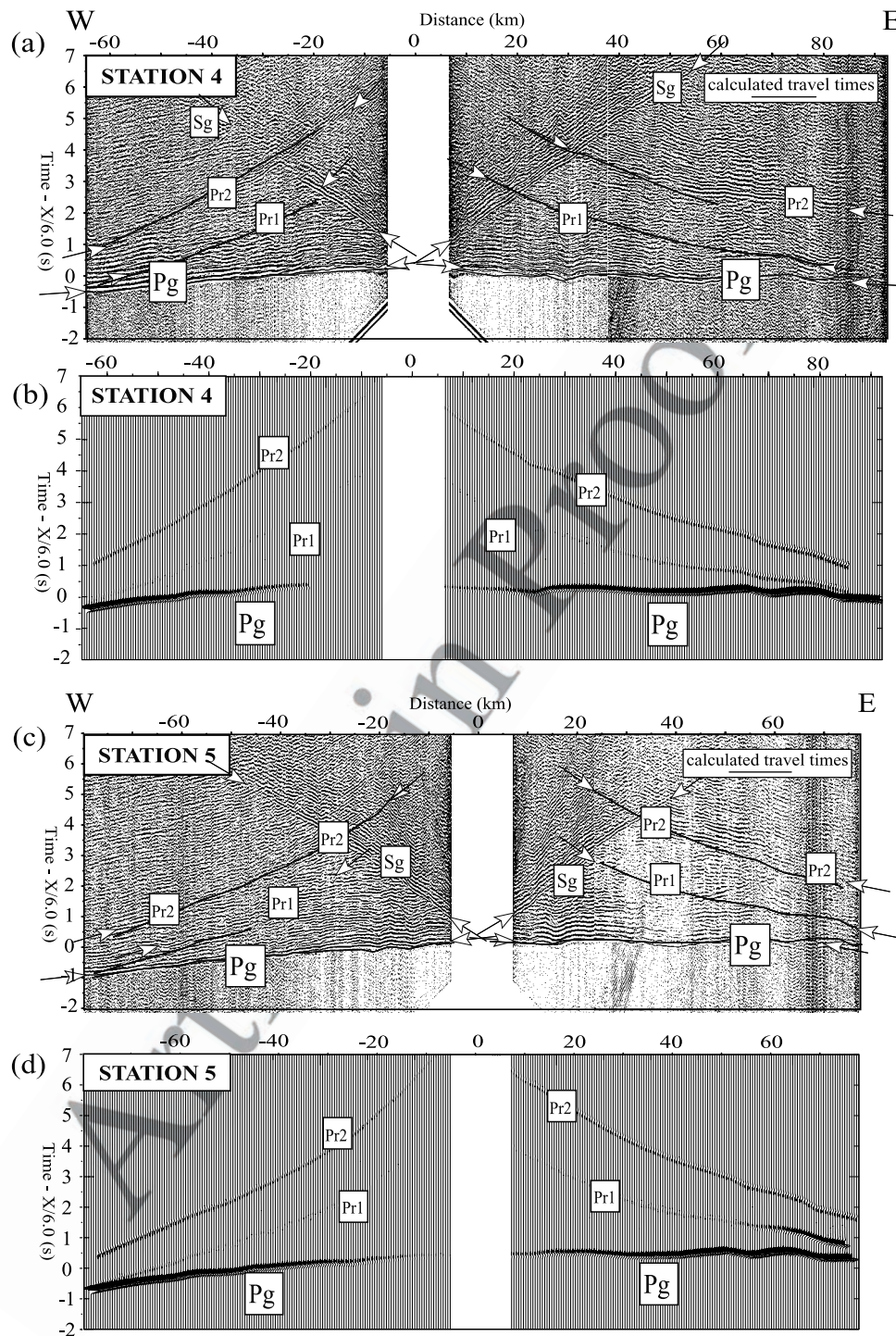


**Figure 3.** Vertical component wide-angle seismic data for the northern Strait of Juan de Fuca. The refraction profiles are plotted with a reduction velocity of  $6 \text{ km s}^{-1}$  and a band-pass filter between 5 and 15 Hz, and amplitudes are scaled proportionally to the square root of offset. Labels indicate the different observed phases. Lines represent calculated travel times. For each station, both the observed data and ray theoretical synthetic seismograms, calculated from the final crustal model, are shown: (a) station 4, observed data; (b) station 4, synthetics; (c) station 5, observed data; and (d) station 5, synthetics.

454 covariance. To explore uncertainty in the velocity at the  
 455 base of layer 4, we perturbed its value from  $7.2$  to  $7.8 \text{ km s}^{-1}$   
 456  $\text{s}^{-1}$  and then inverted for the best fitting depth of *Pr1* for  
 457 each test (Figure 7). For layer 4 arrivals, the RMS misfit and

$\chi^2$  are clearly minimized at a value of  $7.5 \pm 0.1 \text{ km s}^{-1}$ .  
 458 This limited approach, however, provides only a set of  
 459 perturbations of the final model, not an analysis of all  
 460 possible models.  
 461

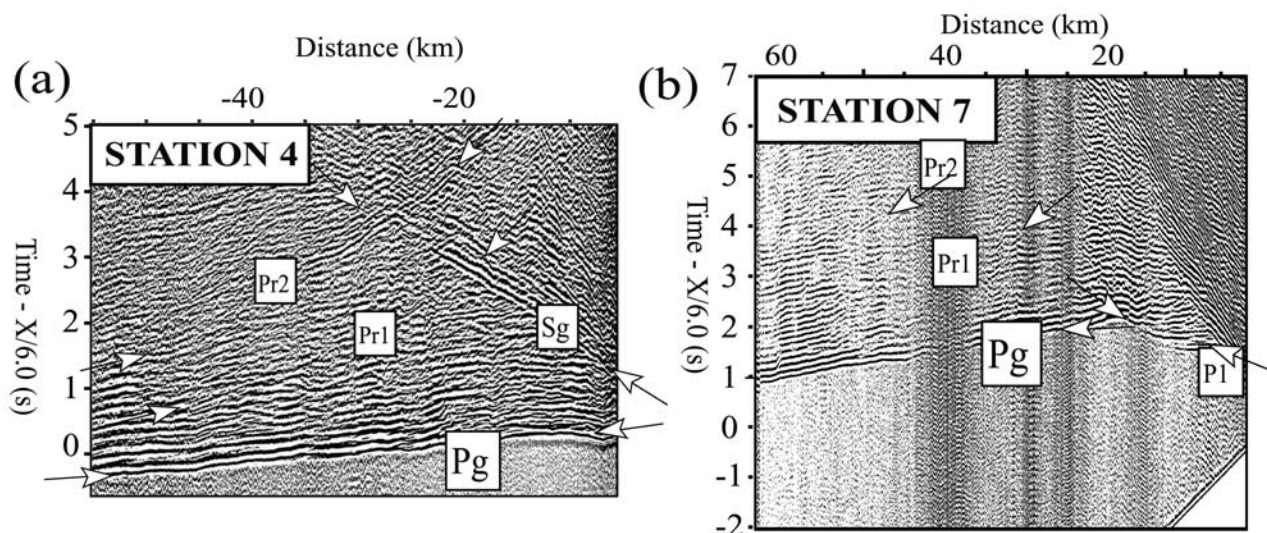


**Figure 4.** Vertical component wide-angle seismic data for the northern Strait of Juan de Fuca. The refraction profiles are plotted with a reduction velocity of  $6 \text{ km s}^{-1}$  and a band-pass filter between 5 and 15 Hz, and amplitudes are scaled proportionally to the square root of offset. Labels indicate the different observed phases. (a) First 60 km of station 4. (b) First 60 km of station 7 revealing a low-velocity arrival from a basin in the eastern Strait of Juan de Fuca.

[25] For layer 5, between the two deep reflectors  $Pr1$  and  $Pr2$ , the resolution of velocity nodes is poorer, probably because we do not observe arrivals from rays turning within this layer. Nevertheless, through an uncertainty analysis of the layer velocity values, we can demonstrate that the  $Pr2$ -reflected arrivals provide meaningful velocity constraints. Assuming that the overlying velocity structure is determined, we perturbed the average layer 5 velocities from  $6.9$  to  $8.0 \text{ km s}^{-1}$  and observed the corresponding RMS misfits. Velocities less than  $6.8 \text{ km s}^{-1}$  are not supported since ray paths to many stations could not be found. A velocity of  $8.0 \text{ km s}^{-1}$  seemed a reasonable upper limit as it represents standard mantle velocity. For a fixed velocity contrast of  $0.4 \text{ km s}^{-1}$  between the top and bottom of the layer, we inverted for the lower reflector depth that best satisfied the  $Pr2$  travel times. The minimum misfit was  $0.203 \text{ s}$  for an average velocity of  $7.6 \text{ km s}^{-1}$  ( $\pm 0.2 \text{ km s}^{-1}$ ) (Figure 8a). For this average velocity, we tried several values of velocity gradients within the layer (Figure 8b); as expected, there is little constraint on the velocity gradient since no turning rays within the layer were observed.

## 5. Southern Model

[26] The southern line consisted of 157 km of air gun shots (line 8) fired along the southern Strait of Juan de

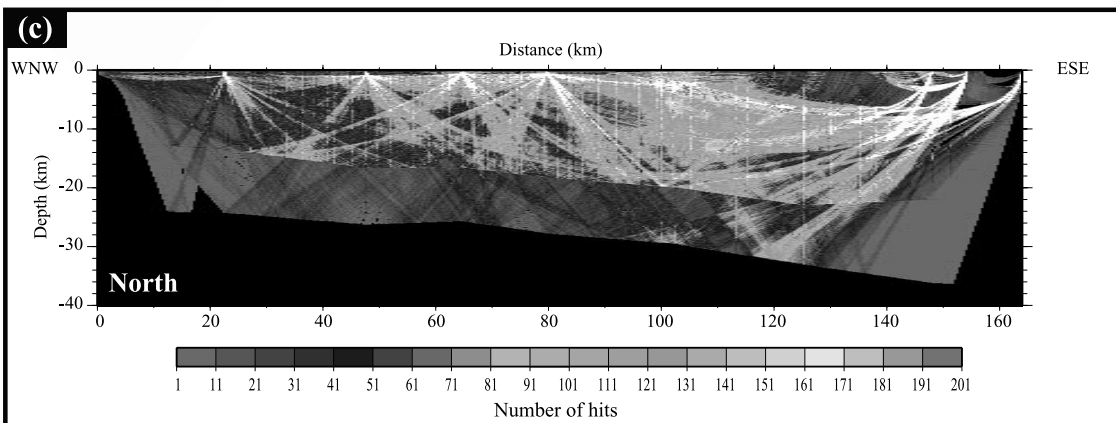
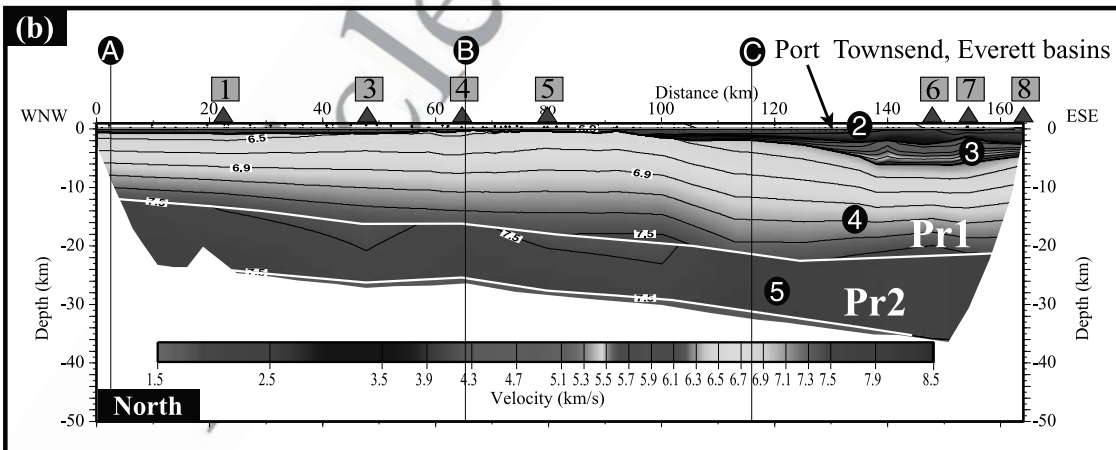
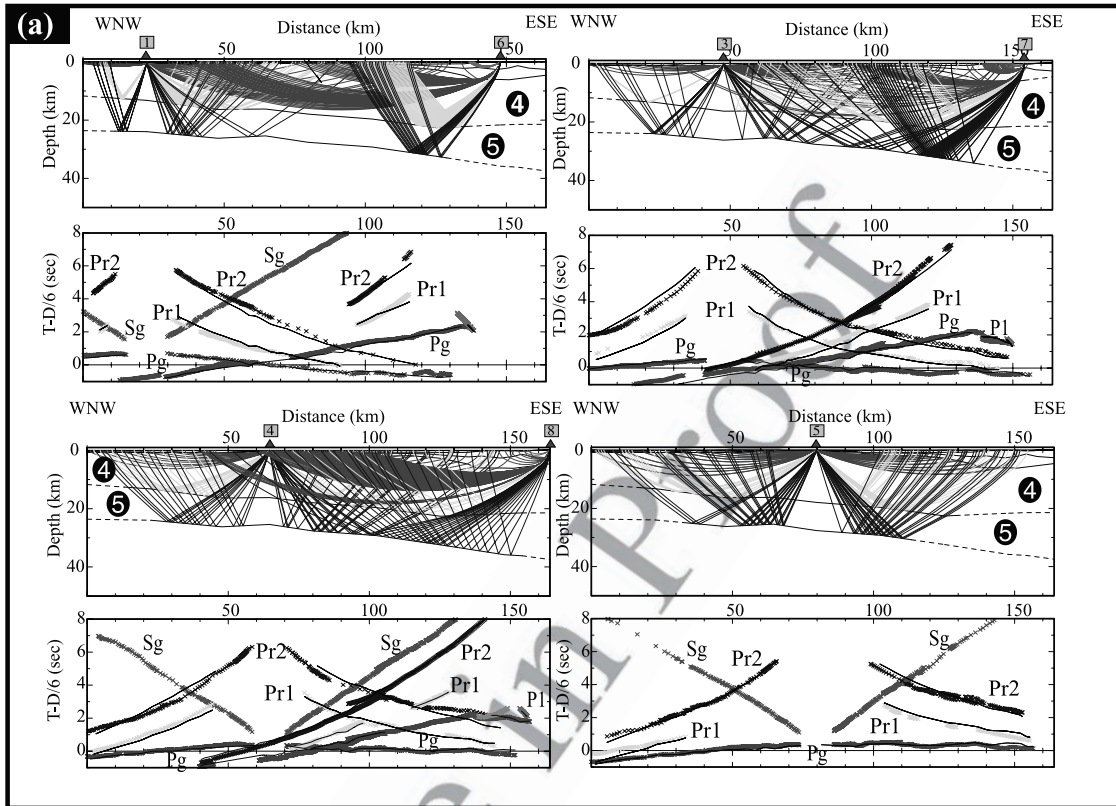
Fuca (Figure 2). We restricted our wide-angle analyses to arrivals at selected Reftek stations a–g deployed on the northern Olympic Peninsula coast. For the first 80 km of the model, the midpoints from shots along line 8 are never off-set by more than 2.5 km from the plane of the model. No Olympic Peninsula stations east of station g were used since nearly all arrivals corresponded to out-of-plane ray paths. The southern model was developed using the same procedure as the northern model except that no amplitude modeling and no estimation of uncertainty of deep velocities was carried out because of the complex pattern of deep-reflectivity-inducing uncertainty in the deeper part of the model. The final model was extended eastward to 157 km by combining it with the eastern part of the northern model.

### 5.1. Wide-Angle Data

[27] On the southern line, arrivals propagated out to offsets of up to 110 km (Figure 9). Five principal phases were observed: a refracted arrival  $P1$  from the upper crust with an apparent velocity of  $4.0$ – $5.0 \text{ km s}^{-1}$ , its associated reflected wave ( $1r$ ), a refraction or turning wave  $Pg$  from the middle crust ( $Pg$ ) with an apparent velocity of  $6.5$ – $7.0 \text{ km s}^{-1}$ , and two groups of reflections ( $Pr2$  and  $PmP$ ) from deep boundaries. At station a (Figure 9a), the weak reflected wave  $1r$  appears to be asymptotic with the

**Figure 5.** (opposite) Northern velocity model. (a) Ray diagrams for the modeled phases and the corresponding observed travel times for stations 1 and 6, 3 and 7, 4 and 8, and 5. The black curves represent calculated travel times. The crosses represent the picked observed arrivals. Different colors correspond to different phases. (b) Velocity model across the northern Strait of Juan de Fuca. Triangles at the top of each velocity model indicate the position of land recording stations.  $Pr1$  and  $Pr2$  refer to wide-angle deep reflectors. Solid circles with white numbers indicate layer numbers given in text. Solid circles with white letters show the position of seismicity (A, B, C), and gravity sections (A, B) perpendicular to the model and shown in Figures 12–14. (c) Number of ray hits for the northern model, which indicates the ray coverage within the model. White color identifies a number of hits greater than 200. See color version of this figure at back of this issue.





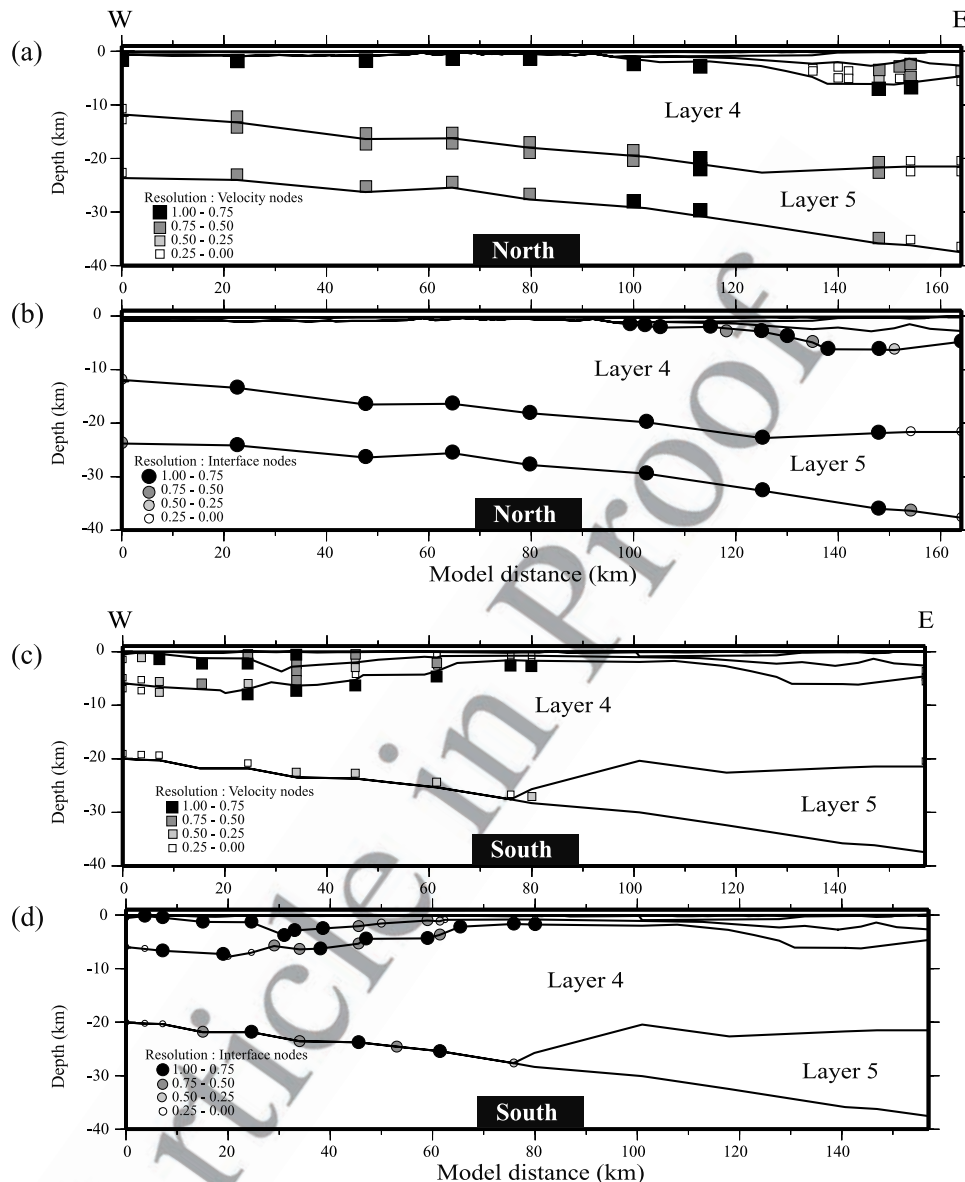


**Figure 6.** Resolution values calculated from the travel time inversion of the northern velocity model: (a) resolution values of the velocity nodes and (b) resolution values of the interface nodes. Same for the southern model: (c) resolution values of the velocity nodes and (d) resolution values of the interface nodes.

512 refracted arrival  $P_1$  around 25 km. From 25 to 110 km, a  
513 strong  $P_g$  arrival is observed.

514 [28] The complex pattern of deep reflectivity, however,  
515 did not allow us to consistently correlate arrivals across all  
516 stations. There was little evidence of a southern equivalent  
517 of  $Pr_1$ , although there are some scattered low-amplitude  
518 reflections. Arrival  $Pr_2$  corresponds to a velocity discontinuity  
519 from a deep reflector.  $PmP$  is a strong reflection  
520 which occurs at approximately 3 s and 100 km on station  
521 a and at 3.5 s and 100 km on stations e and c (Figure 9b),  
522 with an amplitude nearly as large as  $P_g$ . This phase  $PmP$   
523 clearly arrives after  $Pr_2$  at station c (Figure 9c).

## 524 5.2. Velocity Model

525 [29] Wide-angle data modeling produced a compressional  
526  $P$  wave velocity model of the crust below the southern Strait

of Juan de Fuca. This model (Figure 10b) consists of an 527  
upper layer of seawater (layer 1) underlain by a layer of 528  
sedimentary rocks (layer 2) having a maximum thickness of 529  
4 km at around 32-km distance; velocities used for the 530  
shallow sedimentary rocks are  $2.1 \text{ km s}^{-1}$  near the surface, 531  
increasing to  $3.3 \text{ km s}^{-1}$  at the bottom of the layer. Layer 2 532  
is interpreted as a low-velocity sedimentary basin, equivalent 533  
to the Clallam basin of Ramachandran [2001]. Beneath 534  
layer 2, velocities ranging from  $3.8$  to  $5.9 \text{ km s}^{-1}$  in layer 3 535  
may correspond to an upper crustal layer composed of older, 536  
compacted, or weakly metamorphosed sediments. The 537  
thickness of layer 3 reaches 5 km in the west, decreases 538  
to less than 1 km between 80 and 110 km, and increases 539  
again in the eastern part of the model. In the west, layer 3 of 540  
the southern model is equivalent to layer 3 in the northern 541  
model. 542

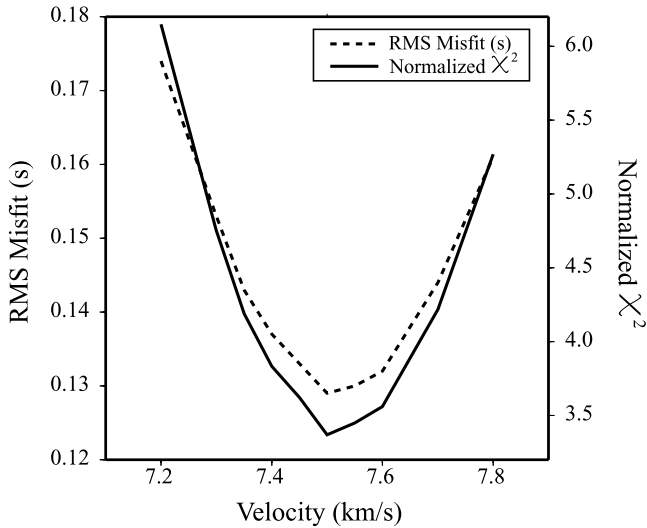


**Figure 7.** Analysis of uncertainty for the velocity at the base of midcrustal layer 4. The RMS misfit and  $\chi^2$  of modeled *Pg*-refracted arrival travel times is plotted as a function of midcrustal layer 4 velocity. A velocity of  $\sim 7.5$   $\text{km s}^{-1}$  minimizes the RMS misfit while allowing rays to be traced to a large number of observations.

[30] The upper to middle crust consists of a thick layer (layer 4), with velocities increasing from 6.0–6.2  $\text{km s}^{-1}$  at its top to 7.5  $\text{km s}^{-1}$  at its base at 20-km depth. A poorly determined wide-angle reflector (*Pr2*) (Table 3 and Figure 10a), deepening from 20-km depth in the northwest to 35 km in the southeast, may represent the base of either layer 4 or 5. Below *Pr2*, the only travel time constraints on velocities can be approached by the observed large amplitude *PmP* reflections, but there is a large trade-off between Moho depth and the velocity in this unit. We did not explore the full range of model space, but the range was sampled by assigning the region between the *Pr2* and *PmP* reflectors three different mean velocities, 6.4, 7.1, and 7.6  $\text{km s}^{-1}$ . A velocity of 6.4  $\text{km s}^{-1}$  is equivalent to a mean oceanic crust velocity and to the E-layer velocity of 6.4  $\text{km s}^{-1}$  derived by Cassidy [1995]. A velocity of 7.1  $\text{km s}^{-1}$  could represent high-velocity underplated material, such as oceanic rocks [Fuis, 1998]. A velocity of 7.6  $\text{km s}^{-1}$  was chosen to explore the case of a southern deep continuity of the high velocities, the possible southward extension of the deep high-velocity layer in the northern strait. The *PmP* reflector ranges in depth from 34 to 39 km in the west and from 41, 43 to 45.5 km in the east (Figure 10b).

### 5.3. Model Uncertainty

[31] The generally close agreement between observed and calculated travel times (Figures 9 and 10a) is characterized by the small RMS misfit and  $\chi^2$  for each arrival (Table 2). Resolution values of velocity and interface nodes were calculated for the western 80 km of the model (Figures 6c and 6d). Arrivals *P1* and *1r* from the deeper portion of layer 3 have small RMS misfits. However, the number of travel times is small, and so the resolution of both velocity and interface nodes

for layer 3 is poor. The number of ray hits (Figure 10c) also indicates that the velocity structure is only adequately constrained down to 15 km. Layer 4, which corresponds to Crescent-Siletz terrane, has the best resolution with a large number of travel times and a RMS misfit of 0.135 s for phase *Pg* (Table 2). Resolution of the deeper velocity nodes of layer 4 is poorer since offsets are too small to allow deep penetration of turning rays. For arrival *Pr2*, RMS values are relatively large because of the difficulty in picking at all stations (Figure 9). Velocity is only poorly constrained by the *PmP* travel times, and so the deep structures of the southern model should be viewed with caution. For the three velocities used between the *Pr2* and *PmP* reflectors, the *PmP* arrival has RMS misfits of 0.085, 0.092, and 0.101 s for velocities of 6.4, 7.1, and 7.6  $\text{km s}^{-1}$ , respectively (Table 3). This limited exploration of model space suggests that the mean velocity between *Pr2* and *PmP* is more likely in the

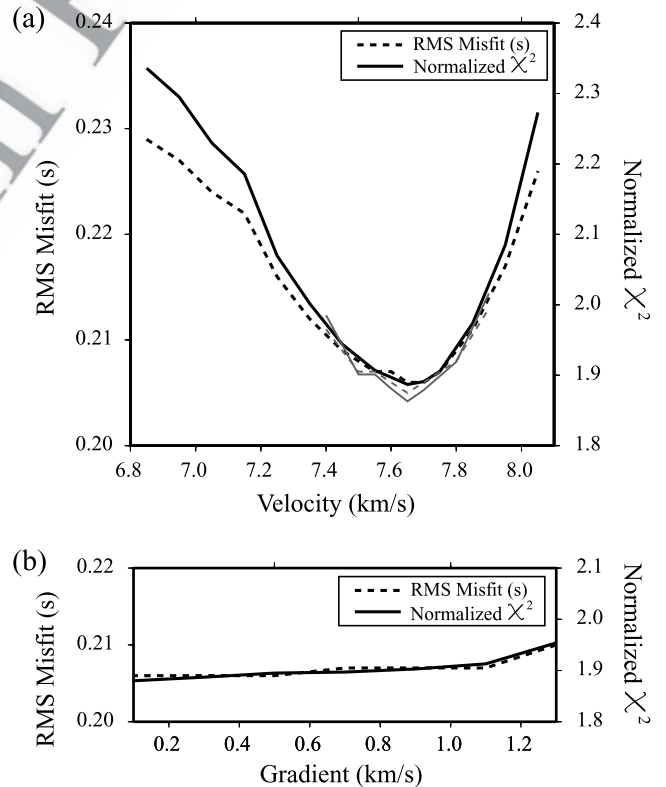


**Figure 8.** Analyses of uncertainty for the velocity and gradient of lower crustal layer 5. (a) RMS misfit and  $\chi^2$  of modeled *Pr2* reflection travel times as a function of velocity at the upper boundary and the lower boundary of layer 5 (black continuous and dashed lines for a velocity gradient of 0.3  $\text{km s}^{-1}$ , shaded continuous and dashed lines for no gradient). A velocity of  $\sim 7.6$ – $7.7$   $\text{km s}^{-1}$  minimizes the RMS misfit while allowing rays to be traced to a large number of observations. RMS misfit implies an uncertainty of  $\pm 0.2$   $\text{km s}^{-1}$  in lower crustal velocities. (b) RMS misfit and  $\chi^2$  of modeled *Pr2* reflection travel times as a function of velocity gradient with an average velocity of 7.65  $\text{km s}^{-1}$ . The flat curve shows that the gradient is not well constrained.

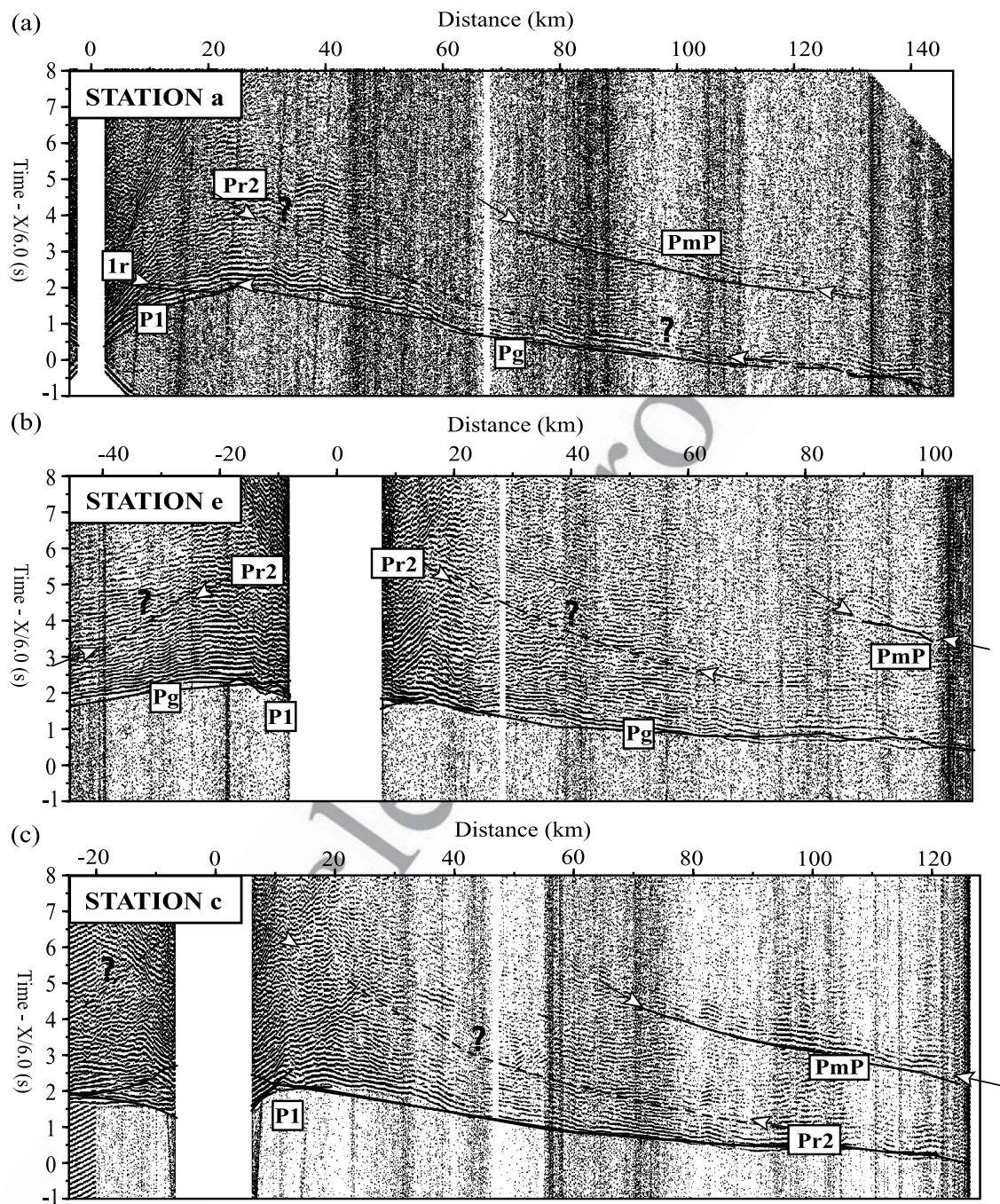
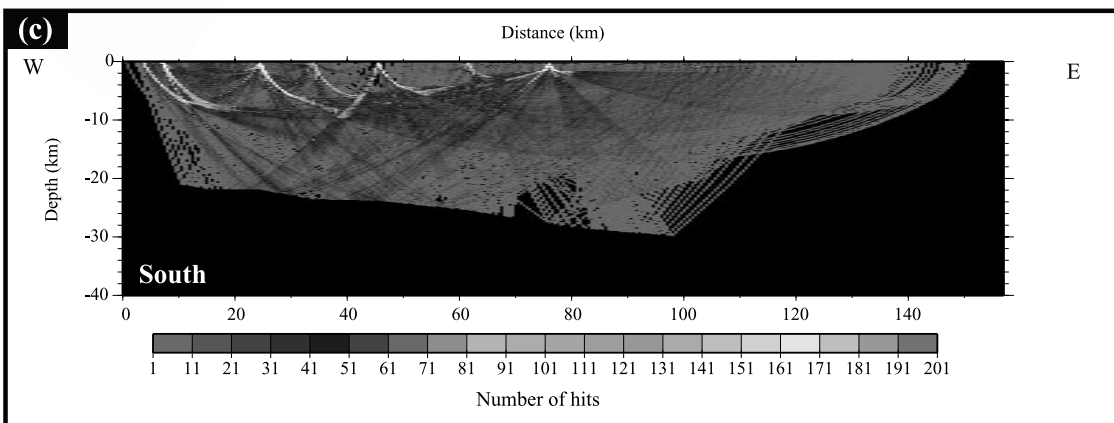
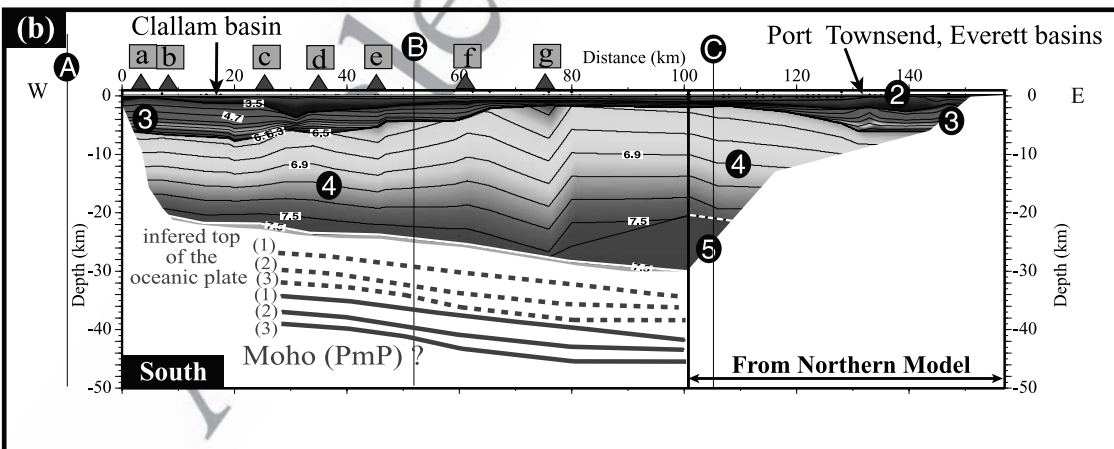
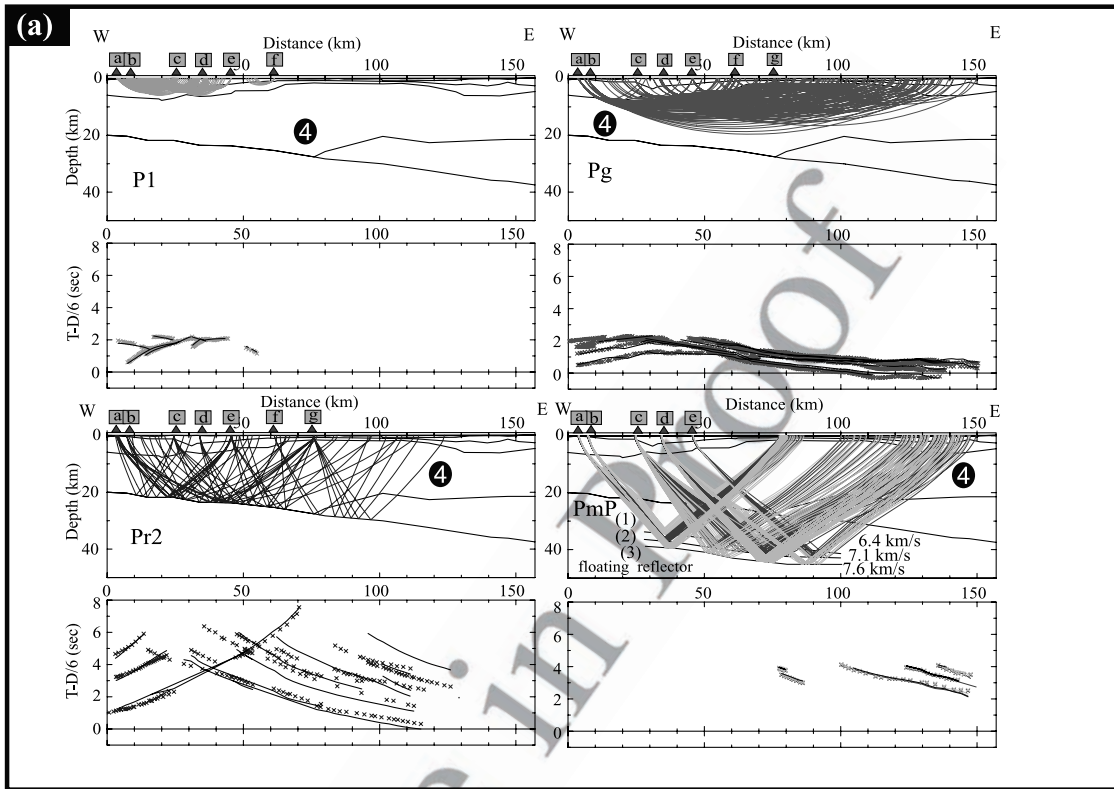


**Figure 9.** Record sections for wide-angle data (vertical component) for the southern Strait of Juan de Fuca. The refraction profiles are plotted with a reduction velocity of  $6 \text{ km s}^{-1}$  and a band-pass filter between 5 and 15 Hz, and amplitudes are scaled proportionally to the square root of offset. Labels indicate the different observed phases. Lines represent calculated travel times. (a) Station a. (b) Station e. (c) Station c.

**Figure 10.** (opposite) Southern velocity model. (a) Ray diagrams for the different modeled phases and the corresponding observed travel times for stations which record different arrivals. The black curves represent calculated travel times. The crosses represent the picked observed arrivals. Different colors correspond to different phases. (b) Velocity model across the southern Strait of Juan de Fuca. Triangles at the top of each velocity model indicate the positions of land recording stations. *Pr2* refers to wide-angle deep reflectors. Solid circles with white numbers indicate layer numbers. Solid circles with white letters show the position of seismicity and gravity sections (A, B, C), perpendicular to the model and shown in Figures 12–14. For the southern model, Moho depths (green lines) are obtained by modeling of *PmP* arrival times, using a velocity between *Pr2* and Moho of either  $6.4 \text{ km s}^{-1}$  (1),  $7.1 \text{ km s}^{-1}$  (2), or  $7.6 \text{ km s}^{-1}$  (3). The eastern part of the southern model, between  $\sim 100$  and 158 km, is identical to the northern model. (c) Number of ray hits for the northern model which translates the ray coverage within the model. White color identifies a number of hits greater than 200. See color version of this figure at back of this issue.



629 range of 6.4–7.1 km s<sup>-1</sup>, with a depth uncertainty at the  
630 Moho of ±1.5 km.

## 632 6. Comparison of Inferred Velocity Models With 633 Three-Dimensional Tomography and Coincident 634 MCS Data

635 [32] Our observations can be extended regionally by  
636 comparing the wide-angle velocity models with coincident  
637 multichannel reflection MCS lines 7 and 8 [Tréhu *et al.*,  
638 2002] and with three-dimensional tomographic models  
639 determined from simultaneous inversion of SHIPS data  
640 and earthquake travel times [Ramachandran, 2001]. As  
641 the three-dimensional tomography depends only on direct  
642 or first-arrival travel times, the current study is able to  
643 provide complementary information since it includes sec-  
644 ondary wide-angle reflected arrivals.

645 [33] The main features in common between MCS line 7  
646 and Lithoprobe Vibroseis line 85-05 are the Leech River  
647 Fault (the boundary between Pacific Rim and Crescent-  
648 Siletz terranes) (Figure 2) and the “reflector band E”  
649 (Figure 11a). Reflector band E is observed as a series of  
650 prominent reflectors extending from 7 to 9.5 s two-way  
651 travel time (TWT). The E reflections have an apparent  
652 global dip toward the east. As was pointed out by Tréhu  
653 *et al.* [2002], SHIPS MCS line 7 shows only weak indica-  
654 tions for reflection *F* or *O* [Calvert and Clowes, 1990;  
655 Hyndman *et al.*, 1990], interpreted as the top of oceanic  
656 crust or the oceanic Moho at around 10-s TWT and 10-km  
657 distance. We identify deeper reflections that we call “*G*”  
658 lying around 12 s (Figure 11a).

659 [34] The northern velocity model was converted to TWT  
660 for comparison with MCS line 7 (Figure 11a). No signifi-  
661 cant reflections are seen on the MCS data in the region of  
662 reflector *Pr1*. In the eastern Strait of Juan de Fuca, there is  
663 close agreement between the sedimentary basin imaged in  
664 the MCS line and the deepening of layers 2 and 3 from the  
665 refraction model over the distance range 100–160 km  
666 (Figure 5b). The base of the sediments inferred from the  
667 wide-angle data agrees well with the depth of the Port  
668 Townsend basin (a 4–5 km thickness of Tertiary sedimentary  
669 rocks [Johnson and Mosher, 2000]) determined from  
670 the three-dimensional tomography of Brocher *et al.* [2000]  
671 and Ramachandran [2001].

672 [35] An important result of our study is the close coinci-  
673 dence of *Pr2* with the top of the E reflector band, particu-  
674 larly over the central half of the MCS line 7. We note that  
675 the amplitude of the *Pr2* reflection is by far the strongest  
676 immediately east of stations 4 and 5 located at 65 and 80 km  
677 model distance, respectively (Figure 3). The reflection  
678 points for these strong arrivals occur over the model  
679 distance ranging from approximately 75 to 120 km and  
680 over the depth range from 26 to 32 km (Figure 5). The  
681 three-dimensional tomography model of Ramachandran  
682 [2001] shows an anomalous high-density body (7.6 km s<sup>-1</sup>)  
683 just above the subducting slab at an equivalent location  
684 off the southeastern tip of Vancouver Island. The top of the  
685 body is at ~26-km depth (~8-s TWT). The feature is  
686 interpreted as an ultramafic body perhaps associated with  
687 Crescent Formation volcanic rocks. The strong *Pr2* ampli-  
688 tudes are probably produced by large velocity contrasts near  
689 the top of this body.

[36] We compared our southern velocity model to SHIPS 690  
MCS line 8 (Figure 11b). There is close coincidence of the 691  
base of sediments inferred from the wide-angle data with the 692  
Clallam basin imaged on the MCS line between 0- and 60-km 693  
model distances in the west. With several kilometers of 694  
sedimentary rock thicknesses in the southern model, this 695  
contrasts with those in the western portion of the northern 696  
model, in which sediment cover over Crescent-Siletz terrane 697  
is very thin. Consistent with the wide-angle data, the E 698  
reflector band amplitude is weaker on MCS line 8 than on 699  
line 7, and its thickness seems smaller than in the north. 700  
However, as in the north, *Pr2* generally appears to be 701  
associated with the deep reflectivity pattern. Modeling the 702  
*PmP* arrival times produces a Moho at about 12-s TWT 703  
(Figure 11b). 704

## 705 7. Comparison of the Wide-Angle Model With 706 Seismicity

[37] The objectives of this comparison are (1) to relate the 707  
upper plate seismicity with the main geological features 708  
identified on the velocity model, (2) to identify the down- 709  
going plate seismicity, and (3) to determine the relation 710  
between the top of this seismicity and the deeper structure 711  
of our wide-angle models, in particular the E reflector band 712  
and the *PmP* reflector. 713

[38] Seismicity presented on the sections of Figure 12 can 714  
be divided into two groups. Most of the seismicity appears 715  
to be concentrated in the upper crust, especially within 716  
Crescent-Siletz terrane. The deeper seismicity occurs within 717  
the downgoing plate. The top of the downgoing Juan de 718  
Fuca plate seismicity was estimated on the three sections. 719  
As there are only few events on section B between 0 and 720  
80 km, the proposed limit of deeper seismicity has a large 721  
uncertainty and was plotted as a dashed line (Figure 12). 722  
The depths where the three sections intersected the northern 723  
and southern velocity models as well as the seismicity 724  
plotted along the velocity models were used to draw the 725  
possible top of downgoing plate seismicity along the two 726  
wide-angle velocity models (Figures 12d and 12e). 727

[39] On the southern model, modeling of *PmP* leads to a 728  
Moho which is between 5 and 7 km deeper than the estimated 729  
top of the downgoing plate seismicity (Figure 12). This 730  
thickness corresponds to the thickness of a normal oceanic 731  
crust [White *et al.*, 1992]. Thus significant portions of the 732  
intraplate seismicity appear to occur above the *PmP* within 733  
the subducting ocean crust. Furthermore, the inferred top of 734  
the downgoing plate appears to lie approximately 5–8 km 735  
deeper than reflector *Pr2*. On the northern model, the relation 736  
between *Pr2* and the top of the seismicity is similar. The top 737  
of the Juan de Fuca plate seismicity increases in depth from 738  
28 km in the west to 45 km in the east (Figure 12d). 739

[40] The E reflector band presents a notable low level of 740  
seismicity (Figure 12d). We converted the time thickness of 741  
the E reflector band on the MCS line 7 to depth using a 742  
velocity of 6.35 km s<sup>-1</sup> as determined by Cassidy and Ellis 743  
[1991] from receiver function analysis. The base of the E 744  
reflector band (dashed gray line in Figure 12d) is very close to 745  
the top of the Juan de Fuca plate seismicity (solid dashed line 746  
in Figure 11d). The difference is never greater than 2 km, 747  
within the uncertainties of estimating the depths of both 748  
seismicity and velocity model interfaces; the agreement 749

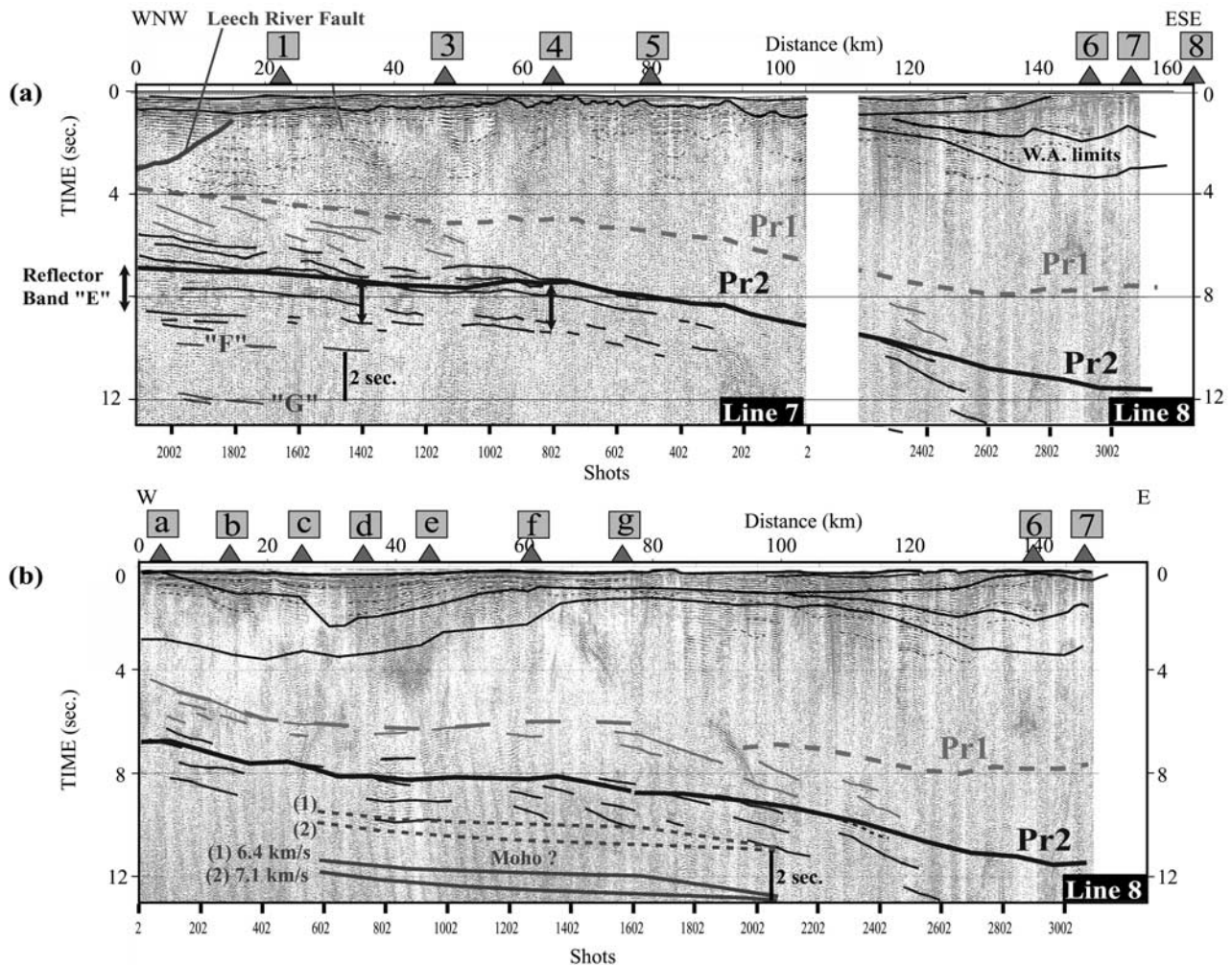


**Figure 11.** Stacked MCS record sections, after preliminary processing, along lines coincident with the wide-angle velocity models. The wide-angle velocity models are converted to time and superimposed on the MCS stacks. Eastern parts of northern and southern models are the same. *Pr1* appears as a gray broken line, and *Pr2* appears as a continuous black line. Thin continuous and broken lines are reflection horizons picked on the MCS record section. “G” refers to deep weak broken reflections around 11-s TWT. (a) SHIPS MCS line 7 coincident with northern model. (b) SHIPS MCS line 8 coincident with southern model. The Moho (shaded) reflection time is calculated from modeling of *PmP* arrival times.

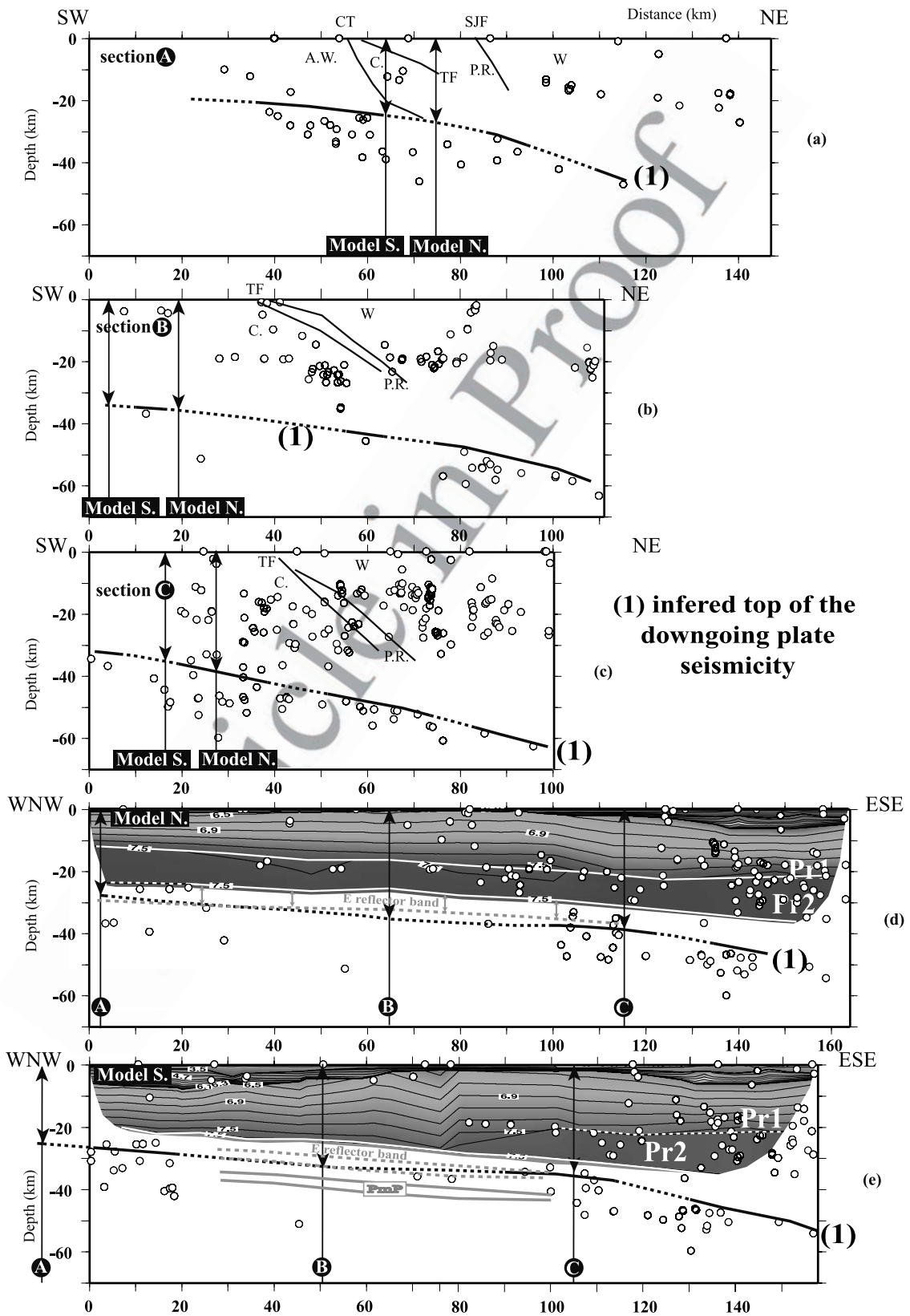
750 would be even better if we used the higher velocity of 7.0–  
 751 7.5 km s<sup>-1</sup> inferred by Ramachandran [2001] for the region  
 752 immediately above the downgoing ocean crust. Knowing the  
 753 large uncertainty of seismicity location, we propose the  
 754 hypothesis that additional underplating beneath the E reflector  
 755 band appears unlikely since the top of the downgoing  
 756 plate appears to coincide approximately with the base of the E  
 757 reflectivity.

## 758 8. Gravity Modeling

### 759 8.1. Procedure

760 [41] Gravity modeling was undertaken to test the inter-  
 761 pretation of the seismic structure data and to extend the  
 762 structure over the entire Strait of Juan de Fuca. The results  
 763 extend those of Dehler and Clowes [1992] and Clowes et al.  
 764 [1997]. To build gravity models, the first constraint is  
 765 provided by the surficial geology (Figure 2). In-depth

structure was first controlled by the geometry at the cross- 766  
 line points with the southern and northern Strait of Juan de 767  
 Fuca wide-angle models (Figures 5b and 10b). Densities 768  
 were inferred using a variety of sources from wide-angle 769  
 seismic velocities for sedimentary rock layers, layer 4 770  
 (Crescent-Siletz terrane), and high-velocity layer 5 (see 771  
 Table 4). We used the appropriate velocity-density relation 772  
 for the relevant types of rocks established by laboratory 773  
 measurements [Ludwig et al., 1970; Nafe and Drake, 1963; 774  
 Carlson and Raskin, 1984; Barton, 1986]. In general, 775  
 densities were consistent with previous gravity modeling 776  
 in the area [Dehler and Clowes, 1992; Clowes et al., 1997], 777  
 modified slightly to fit the additional constraints provided 778  
 by our seismic data. The water layer was assigned density of 779  
 1030 kg m<sup>-3</sup>. The density of Crescent-Siletz formation 780  
 deduced from the wide-angle velocity is 2930 kg m<sup>-3</sup>. This 781  
 value is at the high end of laboratory estimates for Crescent 782  
 rocks reported by Brocher and Christensen [2001], but the 783





t4.1 **Table 4.** Density of Bodies

t4.2	Body	Density, kg m <sup>-3</sup>	Origin
t4.3			<i>Model A</i>
t4.4	Water	1030	
t4.5	Sediments (layer 2)	2110	wide-angle
t4.6	Upper crust (layer 3)	2580	wide-angle
t4.7	Pacific Rim	2800	wide-angle [Dehler and Clowes, 1992; Clowes et al., 1997]
t4.8	Wrangellia	2900	Dehler and Clowes [1992]; Clowes et al. [1997]
t4.9	Crescent Terrane (layer 4)	2930	wide-angle [Brocher et al., 2001]
t4.10	Accreted wedge	2600	Dehler and Clowes [1992]; Clowes et al. [1997]
t4.11	High-density lower crust (Layer 5)	3030	wide-angle
t4.12	E reflector band	2800	Dehler and Clowes [1992]; Clowes et al. [1997]
t4.13	Mantle wedge	3290	Dehler and Clowes [1992]; Clowes et al. [1997]
	Oceanic crust	2890	Dehler and Clowes [1992]; Clowes et al. [1997]; Carlson and Raskin [1984]
t4.14			
t4.15	Oceanic mantle	3330	Dehler and Clowes [1992]; Clowes et al. [1997]
t4.16	Mantle Ast.	3285	Dehler and Clowes [1992]; Clowes et al. [1997]
t4.18			<i>Model B</i>
t4.19	Water	1030	
t4.20	Sediments east (layer 2)	2210	wide-angle
t4.21	Sediments	2110	wide-angle
t4.22	Upper crust (layer 3)	2520	wide-angle
t4.23	Crescent Terrane (layer 4)	2930	wide-angle [Brocher et al., 2001]
t4.24	Accreted wedge	2600	Dehler and Clowes [1992]; Clowes et al. [1997]
t4.25	Pacific Rim	2800	W.A. [Dehler and Clowes, 1992; Clowes et al., 1997]
t4.26	Wrangellia	2900	[Dehler and Clowes, 1992; Clowes et al., 1997]
t4.27	High-density lower crust (layer 5)	3030	wide-angle
t4.28	E reflector band	2800	Dehler and Clowes [1992]; Clowes et al. [1997]
	Oceanic crust	2890	Dehler and Clowes [1992]; Clowes et al. [1997]; Carlson and Raskin [1984]
t4.29			
t4.30	Mantle wedge	3290	Dehler and Clowes [1992]; Clowes et al. [1997]
t4.31	Oceanic mantle	3330	Dehler and Clowes [1992]; Clowes et al. [1997]
t4.32	Mantle Ast.	3285	Dehler and Clowes [1992]; Clowes et al. [1997]

784 seismic model indicates that Crescent velocities and thus  
 785 densities are higher at depth than in the upper few kilometers.  
 786 The forearc upper mantle wedge density is 3290 kg m<sup>-3</sup>.  
 787 This value may be overestimated if the mantle wedge is  
 788 serpentinized as has been recently proposed by Brocher et al.  
 789 [2003] and Blakely et al. [2002]. The reference density used  
 790 to compute gravity anomaly was 3000 kg m<sup>-3</sup> as it represents  
 791 a good central value of used densities. Models have been  
 792 extended 400 km off the ends of the profiles.

793 [42] Lithoprobe and SHIPS crustal reflection lines also  
 794 provide important constraints on the deep structure of the  
 795 Insular Belt and Georgia Strait [Clowes et al., 1987;  
 796 Calvert, 1996; Zelt et al., 2001] (Figure 13). Along section  
 797 B (25–50 km), we based the structure on the interpretation  
 798 of line 84-02 by Clowes et al. [1987] (Figure 14). At model  
 799 distance 68 km, we also used results from receiver function  
 800 analyses undertaken by Cassidy [1995; Cassidy et al., 1998]  
 801 to constrain the thickness of the crust and the position of the  
 802 E reflector band. The thickness of the continental crust was

set to 36–38 km throughout most of the Coast Belt, 803  
 decreasing in the west to 33 km near the Insular Coast Belt 804  
 contact [Zelt et al., 1996; Ramachandran, 2001]. The 805  
 position of the downgoing slab was deduced from the 806  
 previous analysis of seismicity (Figure 12). 807

## 8.2. Modified Explanation for the Gravity High and Results

[43] The most prominent feature of the gravity data 810  
 around Strait of Juan de Fuca (Figure 13) is the gravity 811  
 high located on southeastern Vancouver Island (+65 mGal), 812  
 corresponding roughly to the location where high-density 813  
 igneous Crescent-Siletz terrane rocks crop out. The Coast 814  
 Range Province, which is the southern equivalent of Cres- 815  
 cent-Siletz formation, reaches a thickness of 30 km near its 816  
 eastern edge. With a density of 2920 kg m<sup>-3</sup>, it can explain 817  
 the gravity high in western Washington [Finn, 1990]. A 818  
 large thickness of Crescent-Siletz terrane may also contrib- 819  
 ute to the gravity high on southern Vancouver Island. 820

**Figure 12.** (opposite) Comparison of the 2D velocity model derived from wide-angle data with seismicity. Earthquakes were perpendicularly projected on each line from a distance of 25 km on either side. Labeled bold line indicates the inferred top of the downgoing plate seismicity. We used all the events from microearthquakes around the Strait of Juan de Fuca catalog compiled by Mulder [1995; also personal communication, 2001], with selected magnitude greater than 1 recorded between the years 1984 and 2000. (a) Seismicity along profile A (Figure 10). (b) Seismicity along profile B. (c) Seismicity along profile C. (d) Seismicity along northern model. Bold line indicates the top of the downgoing plate seismicity deduced from perpendicular sections A, B, and C. Dotted shaded line is the base of the “E reflector band,” using a time thickness from MCS section 7 converted to depth with a velocity derived from receiver function analyses of Cassidy [1995]. (e) Seismicity along southern model. Bold line indicates the top of Juan de Fuca plate seismicity. CT, Crescent Thrust; SJF, San Juan Fault; TF, Tofino Fault; A.W., Accreted Wedge; C., Crescent; P.R., Pacific Rim; W, Wrangellia.

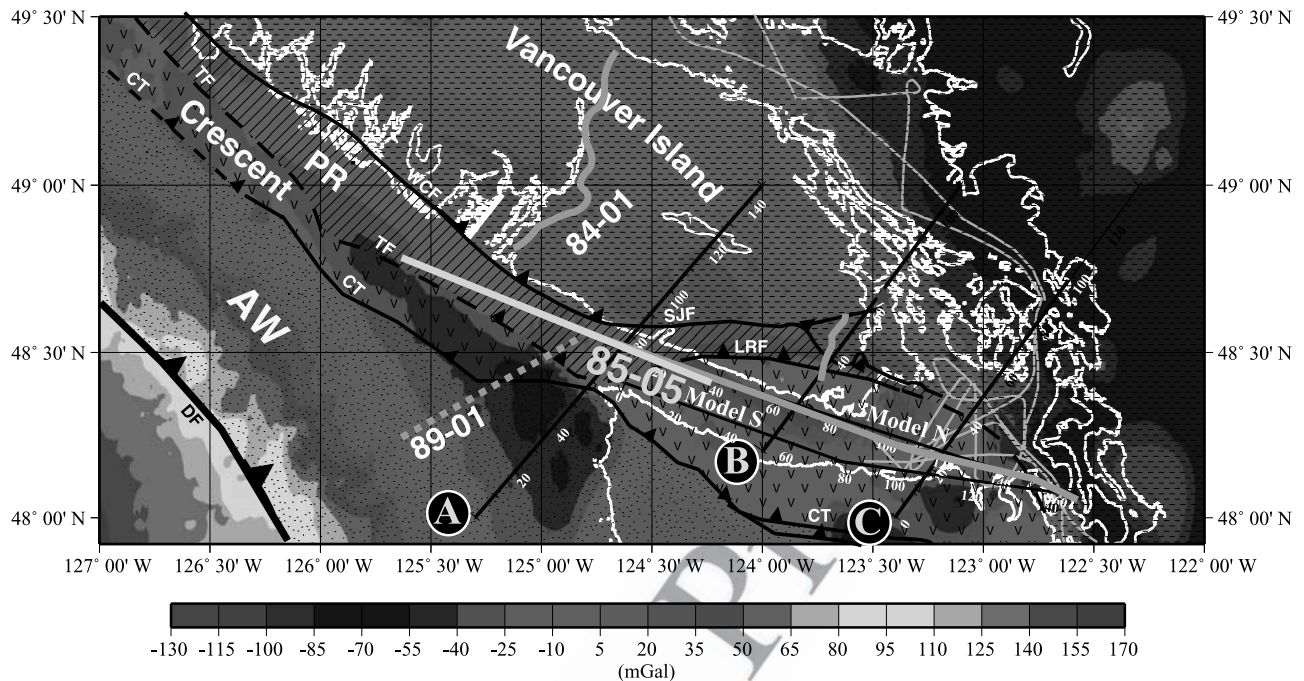


**Figure 13.** Gravity map of the Strait of Juan de Fuca. Data were interpolated to a grid with a grid size of  $0.3 \times 0.3$  min. The three black lines (A, B, and C) indicate the location of modeled gravity profiles (A and B) (Figure 14) and three seismicity sections (A, B, and C) (Figure 12). Shaded lines show location of SHIPS line in Georgia Strait and eastern Juan de Fuca Strait. See color version of this figure at back of this issue.

821 [44] Recognizing the fundamental nonuniqueness of  
 822 gravity interpretations, we adjusted the densities of the  
 823 primary crustal elements (Crescent, high-density lower  
 824 crust, E layer) within reasonable limits to determine the  
 825 approximate sensitivity of the gravity model to density  
 826 changes (Figure 14). A decrease in Crescent density to  
 827  $2800 \text{ kg m}^{-3}$  in general produces a local decrease of the  
 828 central gravity anomaly by about  $\sim 15\text{--}30$  mGal. Alterna-  
 829 tively, an increase in density of the E layer to  $3000 \text{ kg m}^{-3}$ ,  
 830 nearly matching the high density of the lower crustal layer,  
 831 produces an overall increase of about  $\sim 20$  mGal. Charac-  
 832 teristic of gravity modeling, there are many potential trade-  
 833 offs in the crustal density distribution. Our density model  
 834 represents a distribution that is as consistent as possible with  
 835 the seismic velocity constraints. Although we crudely  
 836 attempt to account for three-dimensional variations with  
 837 multiple two-dimensional models, we nevertheless recog-  
 838 nize that unknown three-dimensional effects may be present  
 839 and careful three-dimensional modeling is required.

840 [45] Our modeling shows that the gravity high may be  
 841 consistent with (1) a large thickness of Crescent-Siletz  
 842 terrane beneath the Strait of Juan de Fuca and (2) high-  
 843 velocity and high-density rocks within the lower crust, and  
 844 (3) shallow depth of the subducting ocean crust and mantle  
 845 beneath the Olympic Peninsula and southern Vancouver  
 846 Island. Together, these features produce a large positive  
 847 anomaly in southern Vancouver Island and the northern  
 848 Strait of Juan de Fuca (Figures 13 and 14). A previous  
 849 interpretation of this anomaly by *Dehler and Clowes* [1992]  
 850 assumed that the Crescent-Siletz terrane was less than 7 km  
 851 in thickness. They assumed that the lower 5 km of this unit  
 852 had a density of  $3200 \text{ kg m}^{-3}$ , which may represent high-

density lower crust but is more readily associated with  
 upper mantle material. Our model (Figure 14b) contrasts  
 with this previous result in that Crescent-Siletz terrane has a  
 more normal lower crustal density ( $2930 \text{ kg m}^{-3}$ ), but it is  
 much thicker and extends to nearly 20 km depth, below  
 which occurs a 5–10 km thick layer of possible mantle  
 material. Our modeling shows also that the top of the  
 downgoing slab, lying just beneath the E reflector band in  
 agreement with seismicity, is consistent with observed long  
 wavelength, lower density gravity. In the western Strait of  
 Juan de Fuca, the gravity model is consistent with accreted  
 wedge sediments above the downgoing plate (Figure 14).  
 Both southwestern and eastern Strait of Juan de Fuca  
 sediment basins are included in the gravity models. Con-  
 trasting sediment thicknesses between north and south are  
 consistent with observed gravity data.

## 9. Discussion and Results

### 9.1. Crescent-Siletz Terrane

[46] Beneath the sedimentary rocks the upper crust is  
 mainly composed of Crescent-Siletz terrane tholeiitic  
 basalts (layer 4).  $P_g$  compressional velocities range from  
 $6.2 (\pm 0.1)$  to  $7.5 (\pm 0.1) \text{ km s}^{-1}$ , consistent with basalts  
 [Christensen, 1996]. Furthermore, we have forward mod-  
 eled the shear wave phase  $S_g$  and calculated a Poisson's  
 ratio  $\sigma$  of  $0.25 \pm 0.3$  (Figures 3 and 5). Based on published  
 Poisson ratios for different rock lithologies [Christensen,  
 1996] this value is less than  $\sigma$  for a typical basalt (0.29). A  
 possible explanation of the lowered values is metamorphism  
 of the basalt to greenschist facies for which Christensen  
 [1996] quotes a  $\sigma$  of 0.26. The minimum thickness of

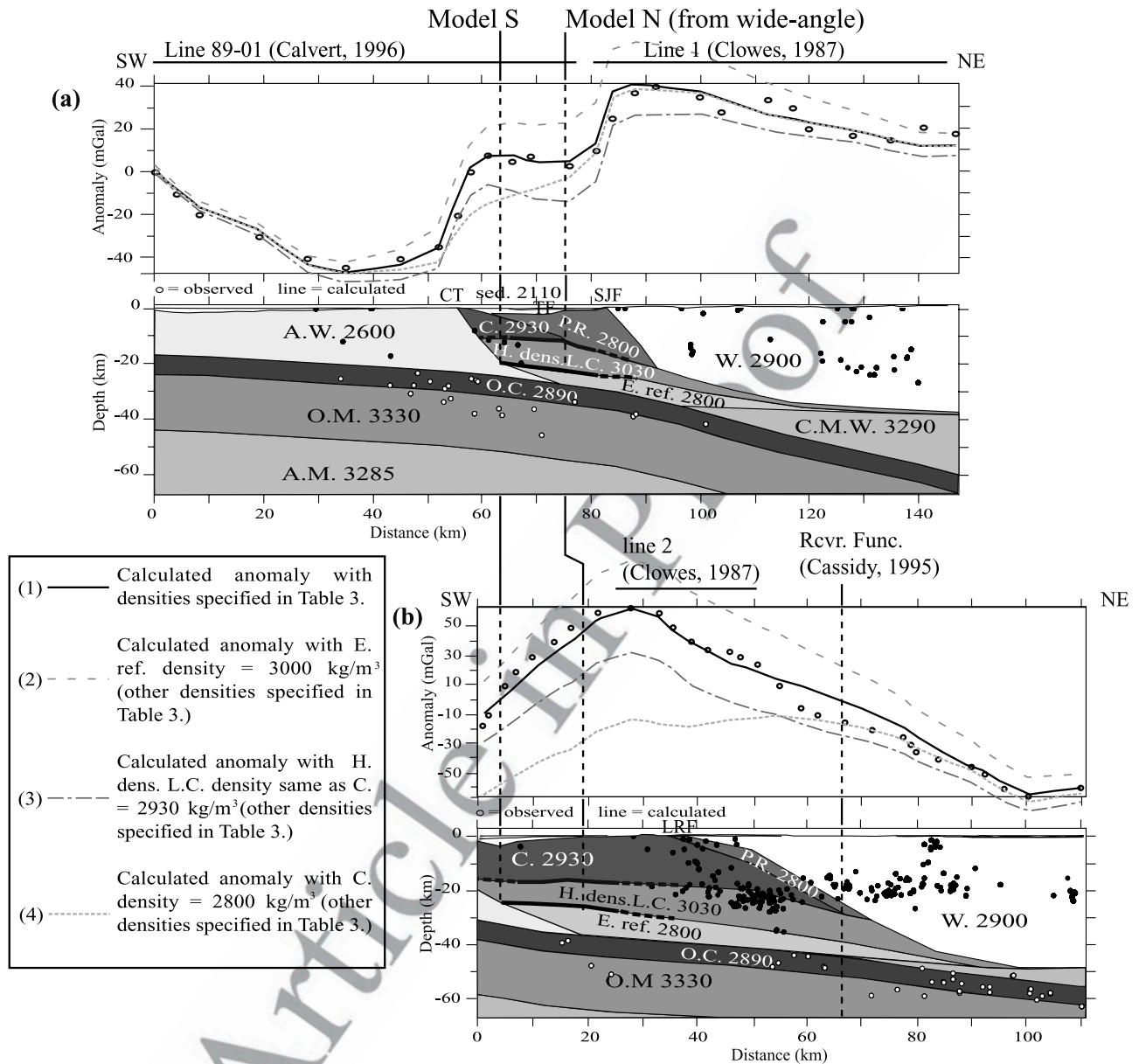


**Figure 14.** Gravity models across the Strait of Juan de Fuca (for location see Figure 13). Densities were deduced from wide-angle velocities for constrained layers. Other densities are consistent with that in the work of Clowes *et al.* [1997], Dehler and Clowes [1992], and Finn [1990]. Some constraints were obtained from MCS Lithoprobe lines and receiver function analyses [Cassidy, 1995]. Heavy, dark shaded line symbolizes Pr1, and heavy black one symbolizes Pr2. Calculated anomalies have desegregated in three steps showing the effect of high-density lower crust, Crescent, and E reflector band. (a) Gravity model along line A in the western Strait of Juan de Fuca. (b) Gravity model along line B in the central Strait of Juan de Fuca. sed., sediments; A.W., accreted wedge; C., Crescent terrane; P.R., Pacific Rim; H. dens. L.C., high-density lower crust; E. ref., E reflector band; O.C., oceanic crust; W., Wrangellia; C.M.W., continental mantle wedge; O.M., oceanic mantle; and A.M., asthenospheric mantle.

884 Crescent-Siletz terrane (12 km in the west and 22 km in the  
885 east) was established from the maximum depth extent of Pg  
886 turning rays and from the additional weak constraint of a  
887 possible reflector Pr1 at the base of the Crescent-Siletz  
888 terrane. South of the study area, Paleocene and Eocene age  
889 accreted oceanic terrane (Siletzia) is comparable or greater  
890 in thickness, reaching 25–35 km beneath the Oregon Coast  
891 Range [Tréhu *et al.*, 1994]. Crescent-Siletz terrane clearly

892 extends north of the Strait of Juan de Fuca, along the  
893 margin, as identified by a strong magnetic anomaly and  
894 by petroleum exploration drill hole sampling [e.g.,  
895 Hyndman *et al.*, 1990]. From multichannel line 85-05 and  
896 several other MCS lines perpendicular to the continental  
897 margin (e.g., 85-01, 89-01, 84-02), the thickness of Cres-  
898 cent-Siletz terrane off Vancouver Island was previously  
899 interpreted as only 6 km [Hyndman *et al.*, 1990; Calvert, 899

1996], typical of normal oceanic crust. However, a large thickness for Crescent-Siletz in the south Vancouver Island region is consistent with recent results from simultaneous inversion of earthquake and SHIPS controlled-source data [Ramachandran, 2001], which suggest that a thicker Crescent-Siletz terrane extends farther north than the mouth of Strait of Juan de Fuca.

## 9.2. Lower Crustal Structure

[47] The lower crustal structure has been determined by mapping the reflector *Pr2*. On the northern section, it lies at a depth of 23 km in the west and 35 km in the east (Figure 5b). Velocities of 7.5–7.7 km s<sup>-1</sup> in layer 5 between *Pr1* and *Pr2*, with an average velocity of 7.6 km s<sup>-1</sup> (Figure 8), are best constrained in the central part of the model. On the coincident MCS reflection line 7, this zone generally has low reflectivity (Figure 11a). An equivalent feature with a velocity of 7.7 km s<sup>-1</sup> at depth ranging from 20 to 25 km was previously identified beneath southern Vancouver Island above the downgoing crust [Spence et al., 1985; Drew and Clowes, 1990]. Ramachandran [2001] also found high-velocity zones beneath the Crescent-Siletz terrane. Furthermore, his three-dimensional velocity models showed that they were generally localized to three regions, including a portion of the Strait of Juan de Fuca, consistent with the present study, and the area beneath southern Vancouver Island to the northwest studied by Spence et al. [1985]. Such high velocities of 7.6 ± 0.2 km s<sup>-1</sup> are inconsistent with a basaltic or gabbroic composition. Having only a weak to no-velocity contrast relative to the Crescent-Siletz terrane, layer 5 is preferably interpreted as a deeper component of Crescent-Siletz, perhaps a thin discontinuous slice of an ultramafic mantle layer that was partially serpentinized or otherwise metamorphosed [Chian and Loudon, 1994; Chian et al., 1995; Godfrey et al., 1997]. As suggested by Ramachandran [2001], the ultramafic layer could be related to the deep mantle source region that produced Crescent-Siletz terrane. Alternatively, layer 5 could have been accreted in a separate event or events as described by Green et al. [1986] and Clowes et al. [1987], a whole underplated slab or remnant of subducted lithosphere perhaps detached when the subduction zone jumped westward to its recent position or an imbricated package of mafic rocks derived by continuous accretion from the top of the subducting oceanic crust.

[48] Reflector *Pr2* is weaker and less continuous in the southern strait (Figure 10b). However, no evidence at all is seen for reflector *Pr1* in the southern strait. Thus high-velocity lower crust or upper mantle material (layer 5), which is evident in the northern model, may be absent in the southern model, and Crescent-Siletz terrane could extend down to reflector *Pr2*. The Crescent-Siletz terrane, with or without its associated ultramafics, may thus reach a thickness of 20 km in southwestern Strait of Juan de Fuca and almost 35 km in the southeast. A similar large thickness for Crescent-Siletz terrane was obtained by Ramachandran [2001] from seismic tomography of SHIPS data on southern Vancouver Island.

## 9.3. E-Reflector Band

[49] The E region of MCS reflectivity is regionally extensive [Clowes et al., 1987] and electrically conductive

[Kurtz et al., 1986, 1990]. It has a pronounced lower density  $\rho = 2800 \text{ kg m}^{-3}$ , a low velocity for *S* waves [Cassidy et al., 1998], and a high Poisson's ratio (0.27–0.38) [Cassidy, 1995]. These attributes support an E zone dominated by thin, fluid-saturated cracks [Cassidy and Ellis, 1991]. There have been two main hypotheses for the origin of the E layer. The first is structural, proposing that the E layer is linked to major faults within the accretionary wedge [Calvert and Clowes, 1990; Calvert, 1996] and truncates at depth a major terrane boundary mapped near the surface. The second hypothesis is that reflectors are caused by fluid-filled porosity created by dehydration reactions associated with changes in metamorphic facies and contrasting physical properties [Hyndman, 1988; Kurtz et al., 1990].

[50] The combined wide-angle seismic, MCS, and seismicity results in the present study contribute to our understanding of the origin of the E layer. The primary results are that (1) reflector *Pr2* is generally associated with the top of the E reflector band (Figures 11 and 12) and (2) the E layer lies just above the top of the subducting oceanic crust as inferred from *PmP* in the southern Strait of Juan de Fuca and from the distribution of Benioff zone seismicity (Figures 12 and 10b). Furthermore, we note that there are apparently no low velocities observed in this region consistent with sheared accretionary sediments, either in the present study or in the study of Ramachandran [2001], within the resolution of the measurements. However, at E-layer depths (>20 km), such sediments may be metamorphosed and their velocities increased. Metamorphic rocks as the origin of E-layer reflectivity cannot be excluded. Alternatively, the E-layer reflectivity may be due to layered, altered serpentinized mafics and ultramafics, perhaps intensely sheared as they are stripped from the downgoing plate and underplated. Located just above the decollement, this sheared zone may provide increased permeability that is filled with fluids under high pressure expelled from the downgoing plate.

## 9.4. Subducting Juan de Fuca Plate

[51] The depths of the oceanic Moho are 35 ± 1.5 km beneath the western strait and 42 ± 1.5 km beneath the eastern strait (Figure 10b). These results are comparable to those of Tréhu et al. [2002] who modeled a Moho at 34–36 km depth beneath western Strait of Juan de Fuca dipping 7° to the east-southeast and at 46 km beneath the eastern Olympic Peninsula. For either of the mean velocities proposed, the Juan de Fuca plate seismicity falls mainly within the oceanic crust (Figures 12d and 12e).

[52] On northern MCS line 7 (Figure 11a), a weak reflector (*G*) occurs beneath the westernmost portion of the line at a depth of 12-s TWT. Since this occurs about 2 s or 6 km beneath the top of the downgoing plate seismicity, we interpret the *G* reflector as the oceanic Moho (Figure 9), i.e., *PmP* in wide-angle data. On Lithoprobe MCS line 84-01, a short reflector (*F*) was observed at 10-s TWT beneath western Vancouver Island. With more continuous observations of oceanic crust farther seaward on GSC line 85-01, reflector *F* was interpreted as the top of the subducting oceanic crust [Hyndman et al., 1990; Calvert, 1996]. This interpretation is consistent with the present modeling of the

1021 new SHIPS seismic data and with the modeling of Tréhu et  
1022 al. [2002].

## 1024 10. Conclusions

1025 [53] SHIPS wide-angle seismic data and gravity modeling  
1026 along the Strait of Juan de Fuca show that the Eocene  
1027 volcanic Crescent-Siletz terrane, which outcrops on south-  
1028 ern Vancouver Island, is much thicker in this region than  
1029 previously interpreted. Beneath the northern strait, a weak  
1030 reflector deepens eastward from 12- to 22-km depth and  
1031 may separate Crescent-Siletz terrane from an associated  
1032 localized mantle root. A deeper, much stronger reflector,  
1033 dipping eastward from 23- to 36-km depth, correlates with  
1034 the top of reflector band E, most likely a shear zone or  
1035 underplated material of alternating mafic/ultramafic layers.  
1036 A high-velocity zone between the two reflectors, well con-  
1037 strained at  $7.6 \pm 0.2 \text{ km s}^{-1}$ , may represent a local lower  
1038 crustal unit of ultramafic mantle, which could be either  
1039 underplated mantle material or the lowermost part of a very  
1040 thick Crescent-Siletz terrane. Beneath the southern strait,  
1041 the E reflector band and the wide-angle midcrustal reflectors  
1042 are less well defined. However, a strong wide-angle reflector  
1043 dipping east from 35 ( $\pm 1.5$ )- to 42 ( $\pm 1.5$ )-km depth may  
1044 be interpreted as the Moho of the subducting ocean crust.  
1045 Seismicity within the Juan de Fuca plate lies mainly above  
1046 the subducting Moho and thus within the subducting  
1047 oceanic crust.

1048 [54] **Acknowledgments.** We thank all the individuals who participated  
1049 in the fieldwork during SHIPS. We also acknowledge Michael Fisher of  
1050 the United States Geological Survey (USGS) as the primary organizer of  
1051 the SHIPS project and for organization of useful meetings with the  
1052 SHIPS Working Group. We thank Taimi Mulder for the providing  
1053 earthquake catalog and helpful discussions at the beginning of this work.  
1054 We thank Carmel Lowe for kindly providing a homogeneous gravity data  
1055 set for the study. We thank the IRIS/PASCAL Data Management Center  
1056 providing easy access to the land station data. Funding for SHIPS was  
1057 primarily through the USGS National Earthquake Hazards Reduction  
1058 Program (NEHERP). The Canadian component was additionally funded  
1059 by the GSC. We are grateful to Tom Brocher and an anonymous reviewer  
1060 for their extensive and very constructive reviews.

## 1061 References

1062 Atwater, B. F., Evidence for great Holocene earthquakes along the outer  
1063 coast of Washington State, *Science*, 236, 942–944, 1987.  
1064 Atwater, B. F., Geological evidence for earthquakes during the past 2000  
1065 years along the Copalis River, southern coastal Washington, *J. Geophys.*  
1066 *Res.*, 97, 1901–1919, 1992.  
1067 Babcock, R. S., R. F. Burmester, D. C. Engebretson, A. Warnock, and K. P.  
1068 Clark, A rifted margin origin for the crescent basalts and related rocks in  
1069 the northern Coast Range volcanic province, Washington and British  
1070 Columbia, *J. Geophys. Res.*, 97, 6799–6821, 1992.  
1071 Barton, P. J., The relationship between seismic velocity and density in the  
1072 continental crust—A useful constraint?, *Geophys. J. R. Astron. Soc.*, 87,  
1073 195–208, 1986.  
1074 Blakely, R. J., T. M. Brocher, and R. E. Wells, Cascadia gravity and mag-  
1075 netic anomalies delineate hydrated forearc mantle, *EOS Trans. AGU*,  
1076 83(47), Fall Meet. Suppl., Abstract S21C-04, 2002.  
1077 Brandon, M. T., Origin of igneous rocks associated with melanges of the  
1078 Pacific rim complex, western Vancouver Island, Canada, *Tectonics*, 8,  
1079 1115–1136, 1989.  
1080 Brandon, M. T., and A. R. Calderwood, High-pressure metamorphism and  
1081 uplift of the Olympic subduction complex, *Geology*, 18, 1252–1255,  
1082 1990.  
1083 Brocher, T. M., and N. I. Christensen, Density and velocity relationships for  
1084 digital sonic and density logs from coastal Washington and laboratory  
1085 measurements of Olympic Peninsula mafic rocks and greywackes, *U. S.*  
1086 *Geol. Surv. Open File Rep.*, 01-264, 29 pp., 2001.  
1087 Brocher, T. M., et al., Wide-angle seismic recordings from the 1998 seismic  
1088 hazards investigation of Puget Sound (SHIPS), western Washington and

British Columbia, U.S. Department of the Interior, *U.S. Geol. Surv. Open*  
1089 *File Rep.*, 99-314, 123 pp., 1999. 1090  
1091 Brocher, T. M., T. Parsons, M. A. Fisher, A. M. Tréhu, G. D. Spence, and  
1092 the SHIPS Working Group, Three-dimensional tomography in the eastern  
1093 Strait of Juan de Fuca: Preliminary results from SHIPS, the 1998 Seismic  
1094 Hazards Investigation in Puget Sound, in *Neotectonics of the Eastern*  
1095 *Juan de Fuca Strait: A Digital Geological and Geophysical Atlas*  
1096 [CD-ROM], edited by D. C. Mosher and S. Y. Johnson, *Geol. Surv.*  
1097 *Can. Open File Rep.*, 3931, 2000. 1098  
1099 Brocher, T. M., T. Parsons, R. J. Blakely, N. I. Christensen, M. A. Fisher,  
1100 R. E. Wells, and the SHIPS Working Group, Upper crustal structure in  
1101 Puget Lowland, Washington: Results from the 1998 Seismic Hazards  
1102 Investigation in Puget Sound, *J. Geophys. Res.*, 106, 13,541–13,564,  
1103 2001. 1104  
1105 Brocher, T. M., T. Parsons, A. M. Tréhu, C. M. Snelson, and M. A. Fisher,  
1106 Seismic evidence for widespread serpentinized forearc upper mantle  
1107 along the Cascadia margin, *Geology*, 31, 267–270, 2003. 1108  
1109 Calvert, A. J., Seismic reflection constraints on imbrication and underplat-  
1110 ing of the northern Cascadia convergent margin, *Can. J. Earth Sci.*, 33,  
1111 1294–1307, 1996. 1112  
1113 Calvert, A. J., and R. M. Clowes, Deep, high-amplitude reflections from a  
1114 major shear zone above the subducting Juan de Fuca plate, *Geology*, 18,  
1115 1091–1094, 1990. 1116  
1117 Calvert, A. J., and R. M. Clowes, Seismic evidence for the migration of  
1118 fluids within the accretionary complex of western Canada, *Can. J. Earth*  
1119 *Sci.*, 28, 542–556, 1991. 1120  
1121 Carlson, R. L., and G. S. Raskin, Density of the ocean crust, *Nature*, 311,  
1122 555–558, 1984. 1123  
1124 Cassidy, J. F., A comparison of the receiver structure beneath stations of the  
1125 Canadian National Seismograph Network, *Can. J. Earth Sci.*, 32, 938–  
1126 951, 1995. 1127  
1128 Cassidy, J. F., and R. M. Ellis, Shear wave constraints on a deep crustal  
1129 reflective zone beneath Vancouver Island, *J. Geophys. Res.*, 96, 19,843–  
1130 19,851, 1991. 1131  
1132 Cassidy, J. F., R. M. Ellis, C. Karavas, and G. C. Rogers, The northern limit  
1133 of the subducted Juan de Fuca plate system, *J. Geophys. Res.*, 103,  
1134 26,949–26,961, 1998. 1135  
1136 Cerveny, V., I. Molotkov, and I. Pšencik, *Ray Method in Seismology*,  
1137 Charles Univ. Press, Prague, 1977. 1138  
1139 Chian, D., and K. E. Loudon, The continent-ocean transition across the  
1140 southwest Greenland margin, *J. Geophys. Res.*, 99, 9117–9135, 1994. 1141  
1142 Chian, D., K. E. Loudon, and I. Reid, Crustal structure of the Labrador Sea  
1143 conjugate margin and implications for the formation of nonvolcanic con-  
1144 tinental margins, *J. Geophys. Res.*, 100, 24,239–24,253, 1995. 1145  
1146 Christensen, N. I., Poisson's ratio and crustal seismology, *J. Geophys. Res.*,  
1147 101, 3139–3156, 1996. 1148  
1149 Clowes, R. M., M. T. Brandon, A. G. Green, C. J. Yorath, A. Sutherland  
1150 Brown, E. R. Kanasevich, and C. Spencer, LITHOPROBE—Southern  
1151 Vancouver Island: Cenozoic subduction complex imaged by deep seismic  
1152 reflections, *Can. J. Earth Sci.*, 24, 31–51, 1987. 1153  
1154 Clowes, R. M., D. J. Baird, and S. A. Dehler, Crustal structure of the  
1155 Cascadia subduction zone, southwestern British Columbia, from potential  
1156 field and seismic studies, *Can. J. Earth Sci.*, 34, 317–335, 1997. 1157  
1158 Dehler, S. A., and R. M. Clowes, Integrated geophysical modelling of  
1159 terranes and other structural features along the western Canadian margin,  
1160 *Can. J. Earth Sci.*, 29, 1492–1508, 1992. 1161  
1162 DeMets, C., R. G. Gordon, D. F. Argus, and S. Stein, Current plate motions,  
1163 *Geophys. J. Int.*, 101, 425–478, 1990. 1164  
1165 Dewey, J. W., D. P. Hill, W. L. Ellsworth, and E. R. Engdahl, Earthquakes,  
1166 faults and the seismotectonic framework of the contiguous United States,  
1167 in *Geophysical Framework of the Continental United States*, edited by  
1168 L. C. Pakiser and W. D. Mooney, *Mem. Geol. Soc. Am.*, 172, 541–576,  
1169 1989. 1170  
1171 Drew, J., and R. M. Clowes, A re-interpretation of the seismic structure  
1172 across the active subduction zone of western Canada—CCSS Workshop  
1173 Topic I, onshore-offshore data set, in *Structures of Laterally Heteroge-*  
1174 *neous Structures Using Seismic Refraction and Reflection Data*, edited  
1175 by A. G. Green, *Pap. Geol. Surv. Can.*, 89-13, 115–132, 1990. 1176  
1177 Duncan, R. A., A captured island chain in the Coast Range of Oregon and  
1178 Washington, *J. Geophys. Res.*, 87, 10,827–10,837, 1982. 1179  
1180 Engebretson, D. C., K. P. Kelley, H. J. Cashman, and M. Richards, 180  
1181 million years of subduction, *GSA Today*, 2, 94–95, 1992. 1182  
1183 Finn, C., Geophysical constraints on Washington convergent margin struc-  
1184 ture, *J. Geophys. Res.*, 95, 19,533–19,546, 1990. 1185  
1186 Fisher, M. A., et al., Seismic survey probes urban earthquake hazards in  
1187 Pacific Northwest, *EOS Trans. AGU*, 80(2), 13, 16–17, 1999. 1188  
1189 Flueh, E. R., et al., New seismic images of the Cascadia subduction zone  
1190 from cruise SO108-ORWELL, *Tectonophysics*, 293, 69–84, 1998. 1191  
1192 Fuis, G. S., West margin of North America—A synthesis of recent seismic  
1193 transects, *Tectonophysics*, 288, 265–292, 1998. 1194

- 1169 Gerdom, M., A. M. Tréhu, E. R. Flueh, and D. Klaeschen, The continental  
1170 margin off Oregon from seismic investigations, *Tectonophysics*, 329, 79–  
1171 97, 2001.
- 1172 Glassey, W., Geochemistry and tectonics of the Crescent volcanic rocks,  
1173 Olympic Peninsula, Washington, *Geol. Soc. Am. Bull.*, 85, 785–794, 1974.
- 1174 Godfrey, N. J., B. C. Beaudoin, S. L. Klemperer, and the Mendocino Work-  
1175 ing Group USA, Ophiolitic basement to the Great Valley forearc basin,  
1176 California, from seismic and gravity data: Implications for crustal growth  
1177 at the North American continental margin, *Geol. Soc. Am. Bull.*, 109,  
1178 1536–1562, 1997.
- 1179 Goldfinger, C., H. Nelson, and J. E. Johnson, Holocene recurrence of  
1180 Cascadia great earthquakes based on turbidite event record, *EOS Trans.*  
1181 *AGU*, 80(46), Fall Meet. Suppl., F1024, 1999.
- 1182 Green, A. G., R. M. Clowes, C. J. Yorath, C. Spencer, E. R. Kanasewich,  
1183 M. T. Brandon, and A. Sutherland Brown, Seismic reflection imaging of  
1184 the subducting Juan de Fuca plate, *Nature*, 319, 210–213, 1986.
- 1185 Heaton, T. H., and S. H. Hartzell, Earthquake hazards on the Cascadia  
1186 Subduction Zone, *Science*, 236, 162–168, 1987.
- 1187 Holbrook, W. S., E. C. Reiter, G. M. Purdy, D. Sawyer, P. L. Stoffa, J. A.  
1188 Austin Jr., J. Oh, and J. Makris, Deep structure of the U.S. Atlantic contin-  
1189 tental margin, offshore South Carolina, from coincident ocean bottom  
1190 and multichannel seismic data, *J. Geophys. Res.*, 99, 9155–9178, 1994.
- 1191 Hyndman, R. D., Dipping seismic reflectors, electrically conductive zones,  
1192 and trapped water in the crust over a subducting plate, *J. Geophys. Res.*,  
1193 93, 13,391–13,405, 1988.
- 1194 Hyndman, R. D., Giant earthquakes of the Pacific Northwest, *Sci. Am.*, 273,  
1195 50–57, 1995a.
- 1196 Hyndman, R. D., The lithoprobe corridor across the Vancouver Island  
1197 continental margin: The structural and tectonic consequences of subduc-  
1198 tion, *Can. J. Earth Sci.*, 32, 1777–1802, 1995b.
- 1199 Hyndman, R. D., C. J. Yorath, R. M. Clowes, and E. E. Davis, The northern  
1200 Cascadia subduction zone at Vancouver Island: Seismic structure and  
1201 tectonic history, *Can. J. Earth Sci.*, 27, 313–329, 1990.
- 1202 Johnson, S. Y., and D. C. Mosher, The eastern Juan de Fuca Strait—Re-  
1203 gional geology map, in *Neotectonics of the Eastern Juan de Fuca Strait: A*  
1204 *Digital Geological and Geophysical Atlas* [CD-ROM], edited by D. C.  
1205 Mosher and S. Y. Johnson, *Geol. Surv. Can. Open File Rep.*, 3931, 2000.
- 1206 Journeay, J. M., and R. M. Friedman, The coast belt thrust system: Evi-  
1207 dence of Late Cretaceous shortening in southwest British Columbia,  
1208 *Tectonics*, 12, 756–775, 1993.
- 1209 Kanamori, H., and T. H. Heaton, The wake of a legendary earthquake,  
1210 *Nature*, 379, 203–204, 1996.
- 1211 Khazaradze, G., A. Qamar, and H. Dragert, Tectonic deformation in wes-  
1212 tern Washington from continuous GPS measurements, *Geophys. Res.*  
1213 *Lett.*, 26, 3153–3156, 1999.
- 1214 Kurtz, R. D., J. M. Delaurier, and J. C. Gupta, A magnetotelluric sounding  
1215 across Vancouver Island detects the subducting Juan de Fuca plate,  
1216 *Nature*, 321, 596–599, 1986.
- 1217 Kurtz, R. D., J. M. DeLaurier, and J. C. Gupta, The electrical conductivity  
1218 distribution beneath Vancouver Island: A region of active plate subduc-  
1219 tion, *J. Geophys. Res.*, 95, 10,929–10,946, 1990.
- 1220 Ludwig, W. J., J. E. Nafe, and C. L. Drake, Seismic refraction, in *The Sea: Ideas and Observations on Progress in the Study of the Seas*, edited by  
1221 A. E. Maxwell, Wiley-Interscience, New York, 1970.
- 1222 Ludwin, R., C. S. Weaver, and R. S. Crosson, Seismicity of the Pacific  
1223 Northwest, in *Neotectonics of North America, Decade of North American*  
1224 *Geology*, vol. GSMV-1, edited by D. B. Slemmons, M. D. Zoback, and  
1225 D. D. Balckwell, pp. 77–88, Geol. Soc. of Am., Boulder, Colo., 1991.
- 1226 Malone, S., R. S. Crosson, K. C. Creager, A. Qamar, G. C. Thomas,  
1227 R. Ludwin, K. G. Troost, D. B. Booth, and R. A. Haugerud, Preliminary  
1228 report on the  $M_w = 6.8$  Nisqually, Washington earthquake of 28 February  
1229 2001, *Seismol. Res. Lett.*, 72, 353–362, 2001.
- 1230 Massey, N. W. D., Metchosin igneous complex, southern Vancouver Island:  
1231 Ophiolite stratigraphy developed in an emergent island setting, *Geology*,  
1232 14, 602–605, 1986.
- 1233 Mazzotti, S., H. Dragert, R. D. Hyndman, M. Miller, and J. Henton, GPS  
1234 deformation in a region of high crustal seismicity: N. Cascadia forearc,  
1235 *Earth Planet. Sci. Lett.*, 198, 41–48, 2002.
- 1236 Miller, K. C., G. R. Keller, J. M. Gridley, J. H. Luetgert, W. D. Mooney, and  
1237 H. Thybo, Crustal structure along the west flank of the Cascades, western  
1238 Washington, *J. Geophys. Res.*, 102, 17,857–17,873, 1997.
- 1239 Mulder, T. L., Small earthquakes in southwestern British Columbia, M. S.  
1240 thesis, Univ. of Victoria, B. C., Canada, 1995.
- 1241 Nafe, J., and C. Drake, Physical properties of marine sediments, in *The Sea*,  
1242 edited by M. N. Hill, pp. 794–828, Wiley-Interscience, New York, 1963.
- 1243 Nedimovic, M. R., R. D. Hyndman, K. Ramachandran, and G. D. Spence,  
1244 Reflection signature of seismic and aseismic slip on the northern Casca-  
1245 dia subduction interface, *Nature*, 424, 416–420, 2003.
- 1246 Parsons, T., A. M. Tréhu, J. H. Luetgert, K. Miller, F. Kilbride, R. E. Wells,  
1247 M. A. Fisher, E. Flueh, U. S. ten Brink, and N. I. Christensen, A new  
1248 view into the Cascadia Subduction Zone and volcanic arc: Implications  
1249 for earthquake hazards along the Washington margin, *Geology*, 26, 199–  
1250 202, 1998.
- 1251 Parsons, T., R. E. Wells, M. A. Fisher, E. Flueh, and U. S. ten Brink, Three-  
1252 dimensional velocity structure of Siletzia and other accreted terranes in  
1253 the Cascadia forearc of Washington, *J. Geophys. Res.*, 104, 18,015–  
1254 18,039, 1999.
- 1255 Ramachandran, K., Velocity structure of south west British Columbia and  
1256 north west Washington, from 3-D non-linear seismic tomography, Ph.D.  
1257 thesis, 198 pp., Univ. of Victoria, B. C., Canada, 2001.
- 1258 Riddiough, R. P., One hundred million years of plate tectonics in western  
1259 Canada, *Geosci. Can.*, 9, 28–34, 1982.
- 1260 Riddiough, R. P., and R. D. Hyndman, The modern plate tectonic regime  
1261 of the continental margin of western Canada, in *Geology of the Cordil-  
1262 leran Orogen in Canada*, edited by H. Gabrielse and C. J. Yorath,  
1263 pp. 435–455, Geol. Surv. of Can., Ottawa, 1991.
- 1264 Rogers, G. C., An assessment of the megathrust earthquake potential of the  
1265 Cascadia subduction zone, *Can. J. Earth Sci.*, 25, 844–852, 1988.
- 1266 Saltus, R. W., and R. J. Blakely, HYPERMAG, an interactive, 2- and 2 1/2-  
1267 dimensional gravity and magnetic modeling program: Version 3.5, *U.S.*  
1268 *Geol. Surv. Open File Rep.*, 93-287, 1–41, 1993.
- 1269 Satake, K., K. Shimazaki, Y. Tsuji, and K. Ueda, Time and size of a giant  
1270 earthquake in Cascadia inferred from Japanese tsunami record of January  
1271 1700, *Nature*, 379, 246–249, 1996.
- 1272 Snavely, P. D., N. S. MacLeod, and H. C. Wagner, Tholeiitic and alkalic  
1273 basalts of the Eocene Siletz River volcanics, Oregon Coast Range, *Am.*  
1274 *J. Sci.*, 266, 454–481, 1968.
- 1275 Spence, G. D., R. M. Clowes, and R. M. Ellis, Seismic structure across the  
1276 active subduction zone of western Canada, *J. Geophys. Res.*, 90, 6754–  
1277 6772, 1985.
- 1278 Stanley, D., and A. Villaseñor, Models of downdip frictional coupling for  
1279 the Cascadia megathrust, *Geophys. Res. Lett.*, 27, 1551–1554, 2000.
- 1280 Stanley, D., A. Villaseñor, and H. Benz, Subduction zone and crustal  
1281 dynamics of western Washington: A tectonic model for earthquake  
1282 hazards evaluation, U.S. Department of the Interior, *U.S. Geol. Surv.*  
1283 *Open File Rep.*, 99-311, 135 pp., 1999.
- 1284 Symons, N. P., and R. S. Crosson, Seismic velocity structure of the Puget  
1285 Sound region from three-dimensional nonlinear tomography, *Geophys.*  
1286 *Res. Lett.*, 24, 2593–2596, 1997.
- 1287 Taber, J. J., and B. T. R. Lewis, Crustal structure of the Washington contin-  
1288 tental margin from refraction data, *Bull. Seismol. Soc. Am.*, 76, 1011–  
1289 1024, 1986.
- 1290 Talwani, M., J. L. Worzel, and M. Landisman, Rapid gravity computations  
1291 for two-dimensional bodies with application to the Mendocino submarine  
1292 fracture zone, *J. Geophys. Res.*, 64, 49–59, 1959.
- 1293 Tréhu, A. M., I. Asudeh, T. M. Brocher, J. H. Luetgert, W. D. Mooney, J. L.  
1294 Nabelek, and Y. Nakamura, Crustal architecture of the Cascadia forearc,  
1295 *Science*, 266, 237–243, 1994.
- 1296 Tréhu, A. M., T. M. Brocher, K. Creager, M. Fisher, L. Preston, G. Spence,  
1297 and the SHIPS 98 Working Group, Geometry of the subducting Juan de  
1298 Fuca plate: New constraints from SHIPS98, *Geol. Surv. Can. Open File*  
1299 *Rep.*, 4350, 25–32, 2002.
- 1300 Van Wagoner, T. M., R. S. Crosson, K. C. Creager, G. Medema, L. Preston,  
1301 N. P. Symons, and T. M. Brocher, Crustal structure and relocated  
1302 earthquakes in the Puget Lowland, Washington, from high-resolution  
1303 seismic tomography, *J. Geophys. Res.*, 107(B12), 2381, doi:10.1029/  
1304 2001JB000710, 2002.
- 1305 Wang, K., Simplified analysis of horizontal stresses in a buttressed forearc  
1306 sliver at an oblique subduction zone, *Geophys. Res. Lett.*, 23, 2021–2024,  
1307 1996.
- 1308 Weaver, C. S., and G. E. Baker, Geometry of the Juan de Fuca plate beneath  
1309 Washington and northern Oregon from seismicity, *Bull. Seismol. Soc.*  
1310 *Am.*, 78, 264–275, 1988.
- 1311 Wells, R. E., C. S. Weaver, and R. J. Blakely, Fore-arc migration in Casca-  
1312 dia and its neotectonic significance, *Geology*, 26, 759–762, 1998.
- 1313 Wheeler, J. O., A. J. Broekefield, H. Gabrielse, J. W. H. Monger, H. W.  
1314 Tipper, and G. J. Woodsworth, Terrane map of the Canadian Cordil-  
1315 lera, *Map 1713A*, scale 1:2,000,000, Geol. Surv. of Can., Ottawa,  
1316 1989.
- 1317 White, R. S., D. McKenzie, and R. K. O’Nions, Oceanic crustal thickness  
1318 from seismic measurements and rare earth element inversions, *J. Geop-  
1319 hys. Res.*, 97, 19,683–19,715, 1992.
- 1320 Yorath, C. J., A. G. Green, R. M. Clowes, A. S. Brown, M. T. Brandon,  
1321 E. R. Kanasewich, R. D. Hyndman, and C. Spencer, Lithoprobe, southern  
1322 Vancouver Island: Seismic reflection sees through Wrangellia to the Juan  
1323 de Fuca Plate, *Geology*, 13, 759–762, 1985.
- 1324 Zelt, C. A., Modelling strategies and model assessment for wide-angle  
1325 seismic traveltimes data, *Geophys. J. Int.*, 139, 183–204, 1999.
- 1326 Zelt, C. A., and R. B. Smith, Seismic traveltimes inversion for 2-D crustal  
1327 velocity structure, *Geophys. J. Int.*, 108, 16–34, 1992.
- 1328

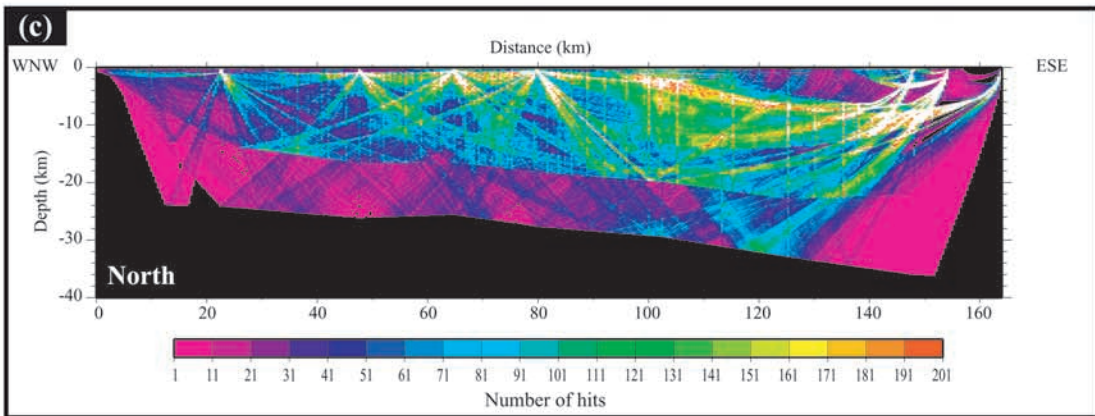
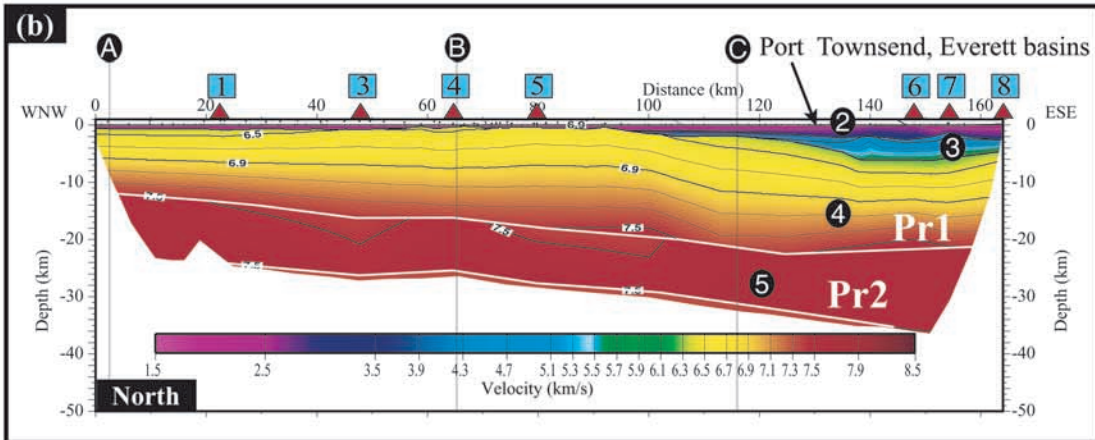
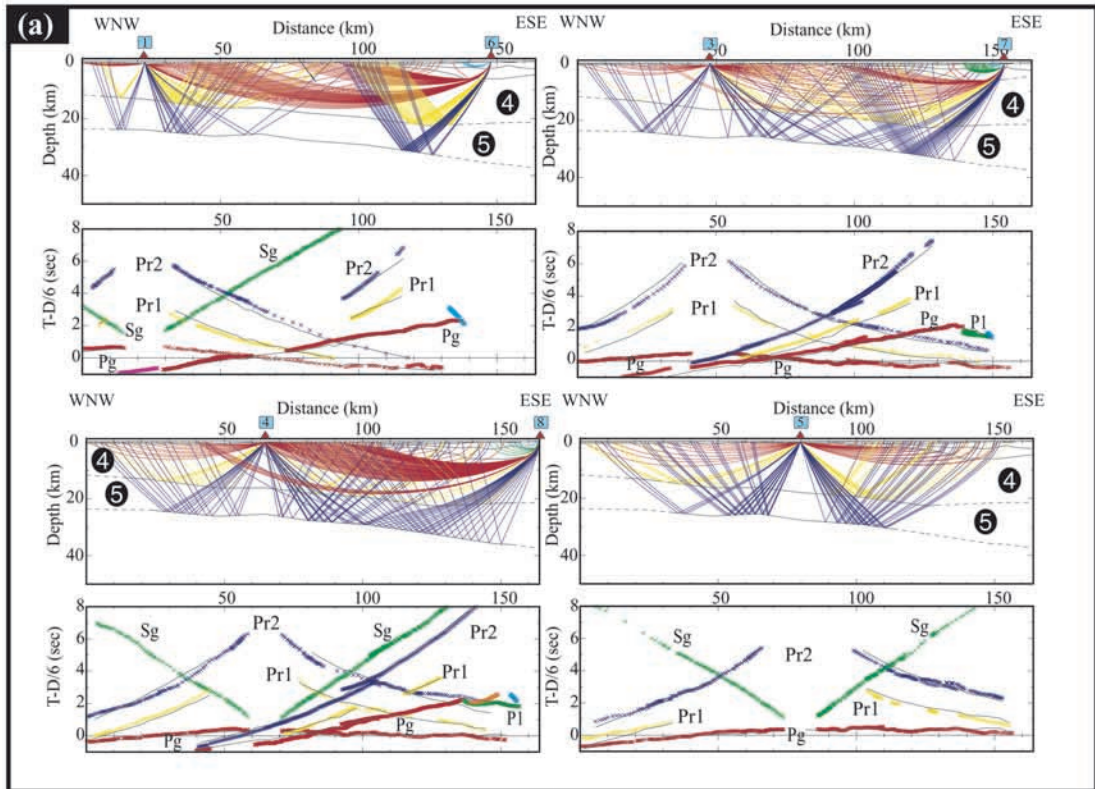
- 1329 Zelt, B. C., R. M. Ellis, R. M. Clowes, and J. A. Hole, Inversion of three-  
1330 dimensional wide-angle seismic data from the southwestern Canadian  
1331 Cordillera, *J. Geophys. Res.*, *101*, 8503–8529, 1996.
- 1332 Zelt, B. C., R. M. Ellis, C. A. Zelt, R. D. Hyndman, C. Lowe, G. D.  
1333 Spence, and M. A. Fisher, Three-dimensional crustal velocity structure  
1334 beneath the strait of Georgia, British Columbia, *Geophys. J. Int.*, *144*,  
1335 695–712, 2001.
- 1337 P. Charvis, J. Y. Collot, and D. Graindorge, UMR Géosciences Azur,  
1338 Observatoire Océanologique de Villefranche sur Mer, B.P. 48, Quai de la  
Darse, F-06235 Villefranche sur Mer, France. (charvis@ccrv.obs-vlfr.fr; 1339  
collot@obs-vlfr.fr; david.graindorge@obs-vlfr.fr) 1340
- R. Hyndman, Pacific Geoscience Center, Geological Survey of Canada, 1341  
Box 6000, Sidney, British Columbia, Canada V8L4B2. (hyndman@pgc. 1342  
nrcan.gc.ca) 1343
- G. Spence, School of Earth and Ocean Sciences, University of Victoria, 1344  
Victoria, British Columbia, Canada V8W 2Y2. (gspence@uvic.ca) 1345
- A. M. Tréhu, College of Oceanic and Atmospheric Sciences, Oregon 1346  
State University, 104 Ocean Administration Building, Corvallis, OR 97331- 1347  
5503, USA. (tréhu@oce.orst.edu) 1348

Article in Proof

Article in Proof

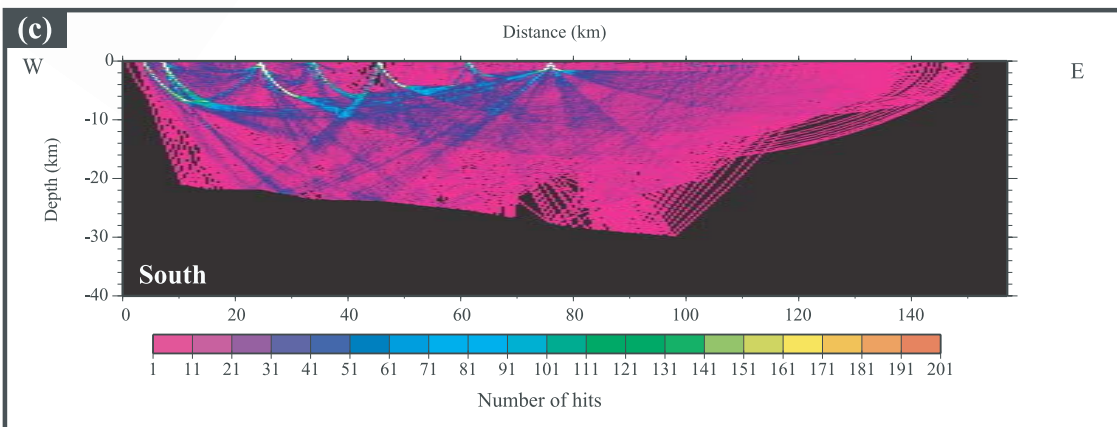
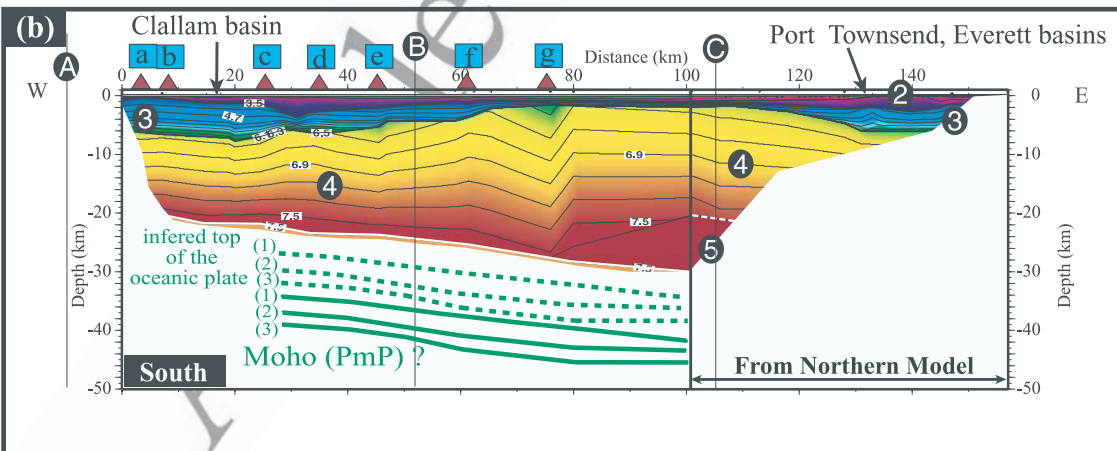
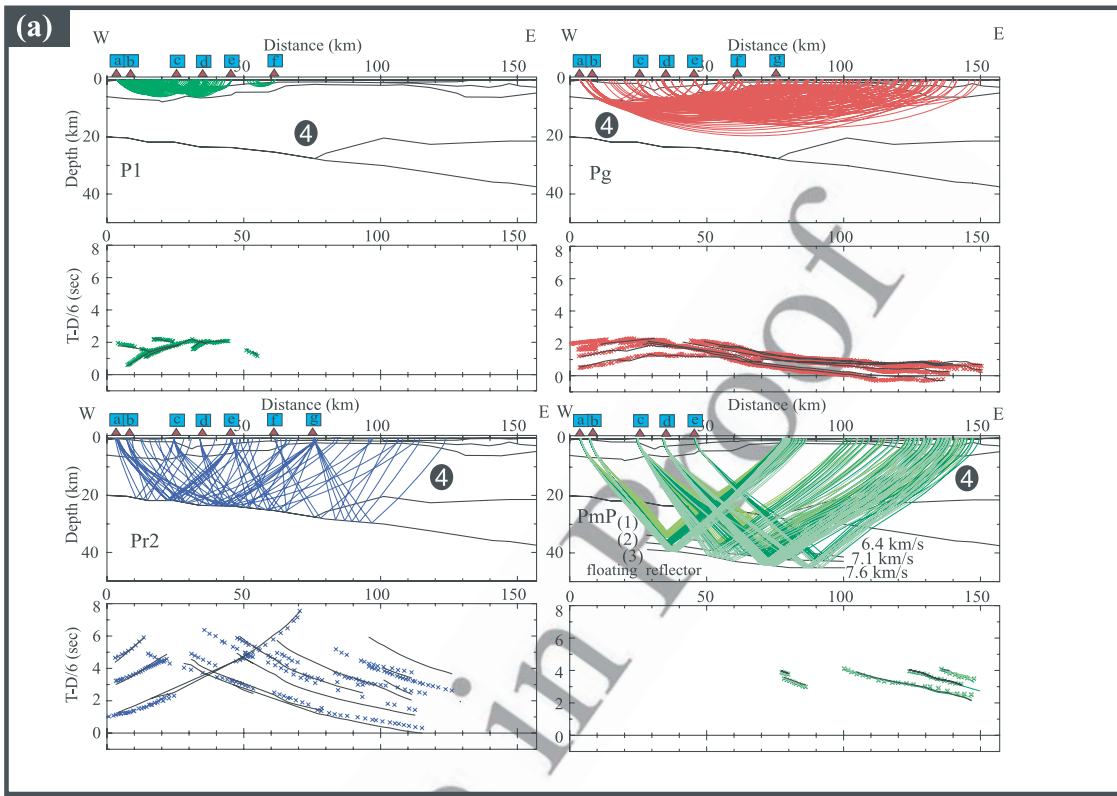
**Figure 5.** (opposite) Northern velocity model. (a) Ray diagrams for the modeled phases and the corresponding observed travel times for stations 1 and 6, 3 and 7, 4 and 8, and 5. The black curves represent calculated travel times. The crosses represent the picked observed arrivals. Different colors correspond to different phases. (b) Velocity model across the northern Strait of Juan de Fuca. Triangles at the top of each velocity model indicate the position of land recording stations. *Pr1* and *Pr2* refer to wide-angle deep reflectors. Solid circles with white numbers indicate layer numbers given in text. Solid circles with white letters show the position of seismicity (A, B, C), and gravity sections (A, B) perpendicular to the model and shown in Figures 12–14. (c) Number of ray hits for the northern model, which indicates the ray coverage within the model. White color identifies a number of hits greater than 200.





Article in Proof

**Figure 10.** (opposite) Southern velocity model. (a) Ray diagrams for the different modeled phases and the corresponding observed travel times for stations which record different arrivals. The black curves represent calculated travel times. The crosses represent the picked observed arrivals. Different colors correspond to different phases. (b) Velocity model across the southern Strait of Juan de Fuca. Triangles at the top of each velocity model indicate the positions of land recording stations. *Pr2* refers to wide-angle deep reflectors. Solid circles with white numbers indicate layer numbers. Solid circles with white letters show the position of seismicity and gravity sections (A, B, C), perpendicular to the model and shown in Figures 12–14. For the southern model, Moho depths (green lines) are obtained by modeling of *PmP* arrival times, using a velocity between *Pr2* and Moho of either  $6.4 \text{ km s}^{-1}$  (1),  $7.1 \text{ km s}^{-1}$  (2), or  $7.6 \text{ km s}^{-1}$  (3). The eastern part of the southern model, between  $\sim 100$  and  $158 \text{ km}$ , is identical to the northern model. (c) Number of ray hits for the northern model which translates the ray coverage within the model. White color identifies a number of hits greater than 200.



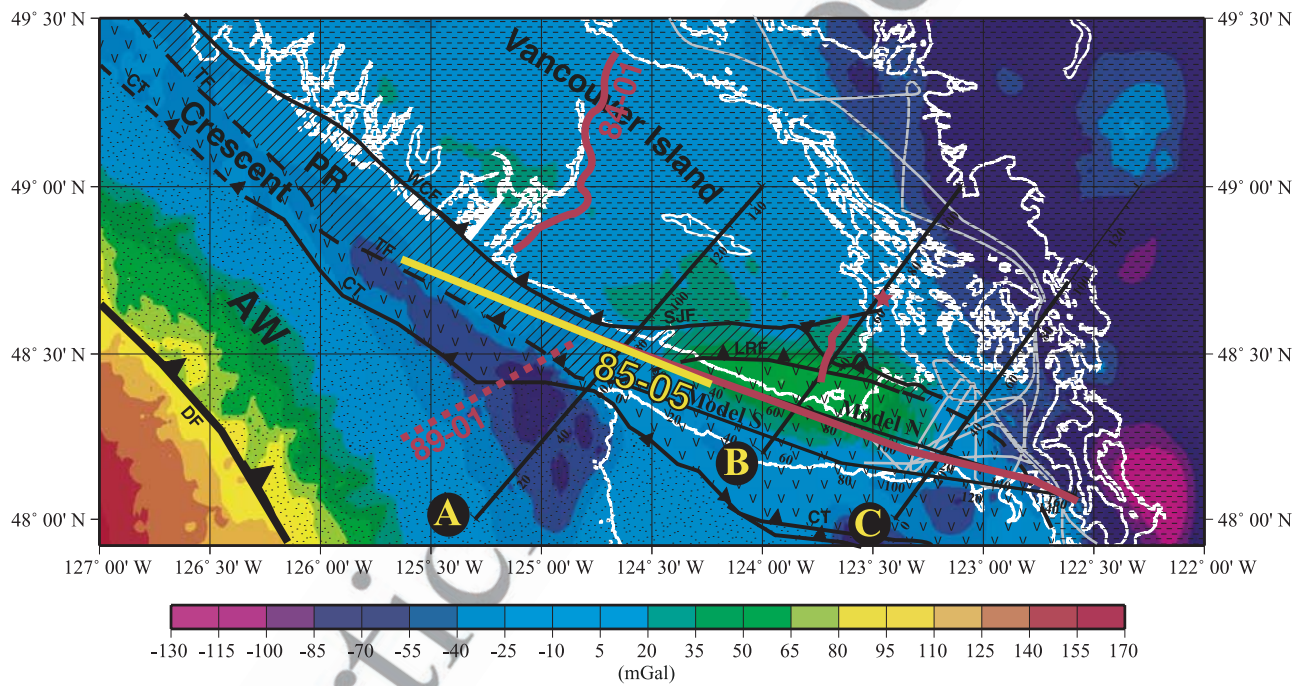


**Figure 13.** Gravity map of the Strait of Juan de Fuca. Data were interpolated to a grid with a grid size of  $0.3 \times 0.3$  min. The three black lines (A, B, and C) indicate the location of modeled gravity profiles (A and B) (Figure 14) and three seismicity sections (A, B, and C) (Figure 12). Shaded lines show location of SHIPS line in Georgia Strait and eastern Juan de Fuca Strait.